

CANDIDATE DISK WIDE BINARIES IN THE SLOAN DIGITAL SKY SURVEY

BRANIMIR SESAR¹, ŽELJKO IVEZIĆ¹, MARIO JURIC²

Draft version October 29, 2018

ABSTRACT

Using SDSS Data Release 6, we construct two independent samples of candidate stellar wide binaries selected as i) pairs of unresolved sources with angular separation in the range $3'' - 16''$, ii) common proper motion pairs with $5'' - 30''$ angular separation, and make them publicly available. These samples are dominated by disk stars, and we use them to constrain the shape of the main-sequence photometric parallax relation $M_r(r-i)$, and to study the properties of wide binary systems. We estimate $M_r(r-i)$ by searching for a relation that minimizes the difference between distance moduli of primary and secondary components of wide binary candidates. We model $M_r(r-i)$ by a fourth degree polynomial and determine the coefficients using Markov Chain Monte Carlo fitting, independently for each sample. Both samples yield similar relations, with the largest systematic difference of 0.25 mag for F0 to M5 stars, and a root-mean-square scatter of 0.13 mag. A similar level of agreement is obtained with photometric parallax relations recently proposed by Jurić et al. (2008). The measurements show a root-mean-square scatter of ~ 0.30 mag around the best fit $M_r(r-i)$ relation, and a mildly non-Gaussian distribution. We attribute this scatter to metallicity effects and additional unresolved multiplicity of wide binary components. Aided by the derived photometric parallax relation, we construct a series of high-quality catalogs of candidate main-sequence binary stars. These range from a sample of $\sim 17,000$ candidates with the probability of each pair to be a physical binary (the “efficiency”) of $\sim 65\%$, to a volume-limited sample of $\sim 1,800$ candidates with an efficiency of $\sim 90\%$. Using these catalogs, we study the distribution of semi-major axes of wide binaries, a , in the $2,000 < a < 47,000$ AU range. We find the observations to be well described by the Öpik distribution, $f(a) \propto 1/a$, for $a < a_{break}$, where a_{break} increases roughly linearly with the height Z above the Galactic plane ($a_{break} \propto 12,300 Z[\text{kpc}]^{0.7}$ AU). The number of wide binary systems with $100 \text{ AU} < a < a_{break}$, as a fraction of the total number of stars, decreases from 0.9% at $Z = 0.5$ kpc to 0.5% at $Z = 3$ kpc. The probability for a star to be in a wide binary system is independent of its color. Given this color, the companions of red components seem to be drawn randomly from the stellar luminosity function, while blue components have a larger blue-to-red companion ratio than expected from luminosity function.

Subject headings: binaries: visual — stars: distances — Hertzsprung-Russell diagram

1. INTRODUCTION

Binary systems can be roughly divided into close (semi-major axes $a \lesssim 10$ AU) and wide (semi-major axes $a \gtrsim 100$ AU, Chanamé 2007) pairs. Close binary systems have long been recognized as useful tools for studies of stellar properties. For example, the stellar parameters such as the masses and radii of individual stars are readily determined to high confidence using eclipsing binaries (Andersen 1991). Wide binary systems have proven to be a tool for studies of star formation processes, as well as an exceptionally useful tracer of local potential and tidal fields through which they traverse. Specifically, they were used to place the constraints on the nature of halo dark matter (Yoo, Chanamé, & Gould 2004) and to explore the dynamical history of the Galaxy (Allen, Poveda, & Hernández-Alcántara 2007). A further comprehensive list of current applications of wide binaries can be found in Chanamé (2007).

Close binaries, owing to their relatively short orbital periods and equally short timescales of bright-

ness or spectrum fluctuations, are fairly easy to detect. Unambiguous identification of wide binary systems, on the other hand, requires accurate astrometry on much longer timescales, as these systems have orbital periods $\gtrsim 10,000$ years. However, instead of requiring unambiguous identification, large samples of *candidate* wide binaries can be selected by simply assuming that pairs of stars with small angular separation are also gravitationally bound (Bahcall & Soneira 1981; Gould 1995), or by searching for common proper motion pairs (Luyten 1979; Poveda et al. 1994; Allen, Poveda, & Herrera 2000; Gould & Salim 2003; Chanamé & Gould 2004; Lépine & Bongiorno 2007). The angular separation method is simple to apply, but it also introduces a relatively large number of false candidates due to chance association of nearby pairs. The contamination by random associations can be reduced by imposing constraints, such as the common proper motion, or by requiring that the stars are at similar distances. The distances can be inferred through a variety of means, one of which is the use of an appropriate photometric parallax³ relation.

The photometric parallax relation provides the abso-

¹ University of Washington, Dept. of Astronomy, Box 351580, Seattle, WA 98195-1580

² Institute for Advanced Study, 1 Einstein Drive, Princeton, NJ 08540

³ Also known as “color-luminosity relation”.

lute magnitude of a star given that star’s color and metallicity. There are a number of proposed photometric parallax relations for main sequence stars in the literature that differ in the methodology used to derive them, photometric systems, and the absolute magnitude and metallicity range in which they are applicable. Not all of them are mutually consistent, and most exhibit significant intrinsic scatter of order a half a magnitude or more (see Figure 2 in Jurić et al. 2008, hereafter J08).

Instead of using an existing relation to select wide binaries, we propose a novel method that *simultaneously* derives the photometric parallax relation *and* selects a sample of wide binary candidates. The method relies on the fact that components of a physical binary have equal distance moduli ($m_1 - M_1 = m_2 - M_1$) and therefore $\delta \equiv \Delta M - \Delta m \equiv (M_2 - M_1) - (m_2 - m_1) = 0$. Assuming that both stars are on the main sequence, and the *shape* of the adopted photometric parallax relation is correct, the difference in absolute magnitudes $\Delta M = M_2 - M_1$ calculated from the parallax relation must equal the measured difference of apparent magnitudes, $\Delta m = m_2 - m_1$. The $\Delta M = \Delta m$ equality for binaries must be valid irrespective of color, and therefore represents a test of the validity of the adopted photometric parallax relation or, alternatively, a way to estimate the parallax relation.

In practice, the distribution of δ will not be a delta-function both due to instrumental (finite photometric precision) and physical effects (true vs. apparent pairs). However, for *true* wide binaries, the distribution of δ is expected to be narrow, strongly peaked at zero, and the individual δ values are expected to be uncorrelated with color. In contrast, the distribution of δ values for randomly associated stellar pairs (hereafter random pairs) should be much broader even when the correct photometric parallax relation is adopted, reflecting the different distances of components of projected binary pairs. This dichotomy can be used to assign a probability to each candidate, of whether it is a true physical binary or a result of chance projection on the sky.

The paper is organized as follows. In Section 2, we give an overview of the SDSS imaging data, and describe the selection, completeness and population composition of two initial, independent samples of candidate binaries. In Section 3 we describe the photometric parallax estimation method, compare the best-fit photometric parallax relations to the J08 relation, and analyze the scatter in predicted absolute magnitudes. The properties of wide binaries, such as the color and spatial distributions, are analyzed in Section 4. Finally, the results and their implications for future surveys are discussed in Section 5.

2. THE DATA

2.1. Overview of the SDSS Imaging Data

Thanks to the quality of its photometry and astrometry, as well as the large sky coverage, the SDSS stands out among available optical sky surveys. The SDSS provides homogeneous and deep ($r < 22.5$) photometry in five bandpasses (u , g , r , i , and z , Gunn et al. 1998; Hogg et al. 2002; Smith et al. 2002; Gunn et al. 2006; Tucker et al. 2006) accurate to 0.02 mag (rms scatter) for unresolved sources not limited by photon statistics (Scranton et al. 2002; Ivezić et al. 2003), and with a zeropoint uncertainty of 0.02 mag (Ivezić et al. 2004).

The survey sky coverage of 10,000 deg² in the northern Galactic cap and 300 deg² in the southern Galactic cap results in photometric measurements for well over 100 million stars and a similar number of galaxies (Stoughton et al. 2002). The recent Data Release 6 (Adelman-McCarthy et al. 2008) lists⁴ photometric data for 287 million unique objects observed in 9583 deg² of sky, and can be accessed through the Catalog Archive Server⁵ (CAS) CasJobs⁶ interface. Astrometric positions are accurate to better than 0.1'' per coordinate (rms) for sources with $r < 20.5$ (Pier et al. 2003), and the morphological information from the images allows reliable star-galaxy separation to $r \sim 21.5$ (Lupton et al. 2002).

The five-band SDSS photometry can be used for very detailed source classification, e.g., separation of quasars and stars (Richards et al. 2002), spectral classification of stars to within one to two spectral subtypes (Lenz et al. 1998; Finlator et al. 2000; Hawley et al. 2002; Covey et al. 2007), identification of horizontal-branch and RR Lyrae stars (Yanny et al. 2000; Sirko et al. 2004; Ivezić et al. 2005; Sesar et al. 2007), and low-metallicity G and K giants (Helmi et al. 2003).

Proper motion data exist for SDSS sources matched to the USNO-B1.0 catalog (Monet et al. 2003). We take proper motion measurements from the Munn et al. (2004) catalog based on astrometric measurements from the SDSS and Palomar Observatory Sky Surveys (POSS-I; Minowski & Abel 1963, POSS-II; Reid et al. 1991). Despite the sizable random and systematic astrometric errors in the Schmidt surveys, the combination of a long baseline (50 years for the POSS-I survey) and a recalibration of the photographic data using positions of SDSS galaxies, results in median random errors for proper motions of only 3 mas yr⁻¹ for $r < 19.5$ (per coordinate), with substantially smaller systematic errors (Munn et al. 2004). Following a recommendation by Munn et al., when using their catalog we select SDSS stars with only one USNO-B match within 1'', and require proper motion rms fit residuals to be less than 350 mas in both coordinates. We note that the proper motion measurements publicly available as a part of SDSS Data Release 6 are known to have significant systematic errors (Munn et al., in prep.). Here we use a revised set of proper motion measurements which will become publicly available as a part of SDSS Data Release 7.

2.2. The Initial Sample of Close Resolved Stellar Pairs

For objects in the SDSS catalog, the photometric pipeline (Lupton et al. 2002) sets a number of flags that indicate the status of each object, warn of possible problems with the image itself, and warn of possible problems in the measurement of various quantities associated with the object. These flags can be used to remove duplicate detections (in software) of the same object, and to select samples of unresolved sources with good photometry.

According to the SDSS Catalog Archive Server “Algorithms” webpage⁷, duplicate detections of the same objects can be removed by considering only those which

⁴ See [HREF]<http://www.sdss.org/dr6>

⁵ [HREF]<http://cas.sdss.org>

⁶ [HREF]<http://casjobs.sdss.org/CasJobs/>

⁷ [HREF]<http://cas.sdss.org/dr6/en/help/docs/algorithm.asp?key=flags>

have the “status” flag set to PRIMARY. We consider only PRIMARY objects, and select those with good photometry by requiring that the BINNED1 flag is set to 1, and PSF_FLUX_INTERP, DEBLEND_NOPEAK, INTERP_CENTER, BAD_COUNTS_ERROR, NOTCHECKED, NOPROFILE, PEAKCENTER, and EDGE image processing flags are set to 0 in the *gri* bands. The moving unresolved sources, such as asteroids, are avoided by selecting sources with the DEBLENDED_AS_MOVING flag set to 0.

Good photometric accuracy (mean PSF magnitude errors < 0.03 mag, see Figure 1 in Sesar et al. 2007) is obtained by selecting sources with $14 < r' < 20.5$, where r' is the *r* band PSF magnitude uncorrected for ISM extinction. The PSF magnitudes corrected for ISM extinction (using maps by Schlegel, Finkbeiner & Davis 1998), and used throughout this work, are noted as *u*, *g*, *r*, *i*, and *z*.

To create the initial sample of resolved stellar pairs, we query⁸ the CAS “Neighbors” table (lists all SDSS pairs within $30''$) for pairs of sources that pass the above criteria, and that have

$$(r_1 - r_2)[(g - i)_1 - (g - i)_2] > 0, \quad (1)$$

where the subscript 1 is hereafter assigned to the brighter component. With this condition we require that the component with bluer *g* – *i* color is brighter in the *r* band. About 40% of random pairs are rejected with this condition. We estimate that about 3% of true binary systems might be excluded by this cut (due to uncertainties in the *g* – *i* color caused by photometric errors), but their exclusion does not significantly influence our results.

We select ~ 4.2 million pairs for the initial sample of resolved stellar pairs, and plot the observed distribution of angular separation θ , $f_{obs}(\theta)$, in Figure 1 (*top*). For a uniform (random) distribution of stars, the number of neighboring stars within an annulus $\Delta\theta$ increases linearly with θ , and therefore, the number of random pairs also increases with θ . To find the number of random pairs as a function of θ , we fit $f_{rnd}(\theta) = C\theta$ to the f_{obs} histogram (in the $\theta > 15''$ region), and find $C = 9043$ arcsec⁻¹. For large separation angles ($\theta > 15''$) the two distributions closely match, indicating that the majority of observed pairs are simply random associations, and are not physically related. At separation angles smaller than $\sim 15''$ the frequency of observed pairs shows an excess, suggesting the presence of true, gravitationally bound systems. However, even at small separation angles, the selected pairs include a non-negligible fraction of random pairs and require further refinement, or careful statistical accounting for random contamination.

Throughout this work we use samples of random pairs (random samples, hereafter) to account for random contamination in candidate binaries. We define the random sample as a sample of pairs with $20'' < \theta < 30''$ taken from the initial pool of stellar pairs. Since pairs in the random sample pass the same data quality selection as candidate binaries, and since virtually all of them are chance associations (99.75%; see Section 4.1 and Figure 1), the random sample is a fair representation of the population of randomly associated stars in candidate binary samples.

⁸ SQL queries are listed in Appendix A

2.3. The Geometric Selection

The excess of pairs with $\theta < 15''$ in Figure 1 (*top*) likely indicates a presence of true binaries, and the angular separation provides a simple, *geometric* criterion to select candidate binary systems. This excess, shown as the ratio f_{obs}/f_{rnd} in Figure 1 (*bottom*), increases for $\theta < 15''$, reaches a relatively flat peak of ~ 1.45 for $3'' < \theta < 4''$, and sharply decreases for $\theta < 2''$ due to finite seeing and inability to resolve close pairs of sources. This excess is related to the fraction of true binaries, $\epsilon(\theta)$, as

$$\epsilon(\theta) = 1 - f_{rnd}(\theta)/f_{obs}(\theta). \quad (2)$$

Using Figure 1 (*bottom*), we choose $3'' < \theta < 4''$ for our geometric selection criterion, since the fraction of true binaries is expected to reach a maximum of $\sim 35\%$ in this range.

The interpretation of the excess of close stellar pairs as gravitationally bound binary pairs implies that the components are at similar distances. If this is true, and if it is possible to constrain the distance via a photometric parallax relation, than their distribution in the color-magnitude diagram should be different than for a sample of randomly associated stars.

To test this hypothesis, we select 51,753 candidate binaries with $3'' < \theta < 4''$. We compare their distribution in the $\Delta r = r_2 - r_1$ vs. $\Delta(g - i) = (g - i)_2 - (g - i)_1$ diagram to the distribution of pairs from the random sample, as shown in Figure 2. The number of pairs in this random sample is restricted to 51,753. Were the selection a random process, the selected candidates would have the same distribution in this diagram as the random sample, and the average candidate-to-random ratio would be ~ 1 . However, in the region where

$$4.33\Delta(g - i) - \Delta r + 0.4 > 0, \quad (3)$$

and

$$2.31\Delta(g - i) - \Delta r - 0.46 < 0 \quad (4)$$

the two distributions are different (average candidate-to-random ratio of ~ 1.7), implying that $> 40\%$ of candidates are found at similar distances. In principle, a selection cut using Equations 3 and 4 could be made to increase the fraction of true binaries in the candidate sample. We do not make such a cut a priori, but instead develop a method (described in Section 3) that robustly “ignores” random pairs while estimating the photometric parallax relation. After a best-fit photometric parallax relation is obtained, the contamination can be minimized by selecting only pairs where both components are at similar distances, as described in Section 4.1.

The *r* vs. *g* – *i* distributions of brighter and fainter components of candidate binaries are shown in Figure 3. We find that the brighter components in the candidate sample are mostly disk G to M dwarfs, while the fainter components are mostly M dwarfs.

2.4. The Kinematic Selection

As seen from Figure 1 (*top*), candidate binaries with $\theta > 15''$ cannot be efficiently selected using angular distance only, as nearly all pairs in this range are most likely chance associations. In this regime, a *kinematic* selection based on common proper motion should be more efficient, as random pairs have a small probability (~ 0.005

determined using Monte Carlo simulations) to be common proper motion pairs (using selection criteria listed below).

We therefore select a second sample of 14,148 candidate binaries by searching for common proper motion pairs with proper motion difference $\Delta\mu = |\mu_2 - \mu_1| < 5$ mas yr^{-1} , and with absolute proper motion in the range $15 \text{ mas } yr^{-1} < |\mu|_{max} < 400 \text{ mas } yr^{-1}$, where $|\mu|_{max} = \max(|\mu_1|, |\mu_2|)$. These criteria require that the directions of two proper motion vectors agree at a 1σ level, and that the proper motion is detected at a 5σ level or higher. The common proper motion pairs with orbital motion $\gtrsim 1''$ over 50 years are not selected because their USNO-B and SDSS positions place them outside the $1''$ search radius used by Munn et al. The angular separation of common proper motion pairs is limited to $9'' < \theta < 30''$. Pairs of sources with $\theta < 9''$ are usually blended in the USNO-B data and may not have reliable proper motion measurements (see Section 4.4), while the maximum angular separation between sources in the CAS “Neighbors” table defines the upper limit of $\theta < 30''$. However, for purposes of Section 4.4, we have created a sample of common proper motion pairs that extends to $\theta = 500''$. We have done so by matching SDSS sources (that pass the quality flags from Section 2.2) within a $500''$ search radius into common proper motion pairs. Since this matching is computationally expensive, we have done this only for one sample. The r vs. $g - i$ distributions of brighter and fainter components of kinematically-selected candidate binaries are similar to those shown in Figure 3.

2.5. The Sample Completeness

Before proceeding with the determination of photometric parallax relations and discussion of the properties of wide binary systems, we summarize the completeness of geometric and kinematic samples, and estimate their expected fractions of disk and halo populations. The samples are selected from a highly-dimensional space of measured parameters and an understanding of the selection effects is a prerequisite for determining the limitations of various derived statistical properties. For example, the geometric sample is selected using five parameters: the $g - i$ color of the two components, $(g - i)_1$ and $(g - i)_2$, their apparent magnitudes, r_1 and r_2 , and their angular separation on the sky, θ . The latter three can be transformed with the aid of a photometric parallax relation into a difference of their apparent magnitudes, $\Delta m = r_2 - r_1$, distance D , and the projected physical separation, a . We seek to constrain the photometric parallax relation by minimizing the difference $\delta = \Delta M - \Delta m$, where ΔM is a two-dimensional function of $(g - i)_1$ and $(g - i)_2$ (Section 3), and at the same time derive constraints on the two-dimensional color distribution of wide binaries, on their a distribution, and on any variation of these distributions with position in the Galaxy (Section 4). Not all of these constraints can be derived independently of each other, and most are subject to severe selection effects. By judiciously selecting data subsets and projections of this five-dimensional parameter space, these effects can be understood and controlled, as described below.

To illustrate the most important selection effects, we employ the photometric parallax relation and its dependence on metallicity derived by Ivezić et al. (2008a, here-

after I08a). The quantitative differences between their photometric parallax relation and the ones derived here have negligible impact on the conclusions derived in this Section. For simplicity, we select a sample of ~ 2.8 million stars with $r < 21.5$ observed towards the north Galactic pole ($b > 70^\circ$), and study their counts as a function of distance and the $g - i$ color. Due to this choice of field position, the distance to each star is approximately equal to its distance from the Galactic plane (for a detailed study of the dependence of stellar number density on position within the Milky Way, see J08). Figure 4 illustrates several important selection effects.

First, for any $g - i$ color there is a minimum and maximum distance corresponding to the SDSS saturation limit at $r \sim 14$ and the adopted faint limit at $r = 21.5$; the probed distance range extends from 100 pc to 25 kpc. Within the distance limits appropriate for a given color, the sample is essentially complete ($\sim 98\%$, Finlator et al. 2000). Second, these limits are strongly dependent on color: the bluest stars saturate at a distance of about 1 kpc, while the reddest stars are too faint to be detected even at a few hundred pc. Equivalently, due to the finite dynamic range of SDSS apparent magnitudes, there is no distance range where the entire color range from the blue disk turn-off edge to the red edge of luminosity function is completely covered. At best, at distances of about 1 kpc the color completeness extends from the blue edge to the peak of luminosity function at $g - i \sim 2.7$. Third, when pairing stars into candidate binary systems, their color distribution at a given distance (the requirement that the differences of apparent and absolute magnitudes are similar places the two stars from a candidate pair into a narrow horizontal strip in the distance modulus (DM) vs. $g - i$ diagram shown in Figure 4) will be clipped: the ratio of the number of candidate binaries and the number of all single stars in the sample decreases at distances significantly different from ~ 1 kpc because of a bias against blue-red pairs.

The binary samples selected from the ~ 1 kpc distance range can be used to measure the two-dimensional color distribution of wide binaries, as well as to gauge the dependence of their a distribution on color. The dependence of the a distribution on distance from the Galactic plane can also be studied over a substantial distance range, but *only under the assumption that it is independent of color*.

The imposed θ range ($3''$ to $30''$) limits the range of probed physical separation to values proportional to distance, and ranging from 3,000 AU to 30,000 AU at a distance of 1 kpc. We discuss and account for these effects in more detail in Section 4.3.

2.6. The separation of disk and halo populations

The counts of main-sequence stars shown in Figure 4 include both disk and halo populations. With the available data, there are three methods that might be used for separating stars (including candidate binary systems) into disk and halo populations (Jurić et al., in prep.):

1. A statistical method based on the stellar number density profiles (J08): beyond about 3 kpc from the plane, halo stars begin to dominate. However, as shown in Figure 4, only stars bluer than $g - i = 2$ are detected at such distances. The stellar number

density profiles suggest that the fraction of halo stars is below $\sim 20\%$ closer than 1.5 kpc from the Galactic plane (see Figure 6 in I08a).

2. Classification based on metallicity into low-metallicity ($[Fe/H] < -1$) halo stars and higher metallicity stars. As shown by I08a, this is a robust and accurate method even when using photometric metallicity estimator, but it works only for stars with $g - i \lesssim 0.7$ due to the limitations of the photometric metallicity method, and the SDSS spectroscopic metallicity is available only for a small fraction of stars in the candidate samples.
3. Kinematic selection based on proper motion measurements, and implemented via a reduced proper motion diagram (e.g., Salim & Gould 2003; Munn et al. 2004, and references therein). However, as discussed in detail in Appendix B, this method is robust only closer than 2-3 kpc from the Galactic plane due to a rotational velocity gradient of disk stars which diminishes kinematic differences between halo and disk stars further away from the plane.

Given the limitations of these methods, it is not possible to reliably separate disk and halo populations throughout the explored parameter space, and in both geometric and kinematic samples. For geometric sample, the third method is not applicable because SDSS-POSS proper motions are not reliable at small angular distances ($\theta \lesssim 9''$; see Section 4.4). The requirement $g - i \lesssim 0.7$ required for the second method results in a subsample with too narrow a color range to constrain the photometric parallax relation. Nevertheless, the analysis of this subsample based on results from I08a indicates that fewer than 10% of stars in geometric sample belong to halo population (this fraction increases with the distance from the Galactic plane; see Figure 6 in I08a), and thus we expect that halo contamination plays only a minor role in the geometric sample.

The kinematic sample is expected to include a non-negligible fraction of halo stars due to the selection of stars with substantial proper motions. We use the reduced proper motion diagram to estimate the fraction of halo candidate binary stars in this sample. The reduced proper motion for an arbitrary photometric bandpass, here r , is defined as

$$r_{RPM} = r + 5 \log(\mu), \quad (5)$$

where μ is proper motion in arcsec yr^{-1} (sometimes an additional offset of 5 mag is added). Using a relationship between proper motion, distance and tangential velocity,

$$v_t = 4.47 \mu D \quad (6)$$

and

$$r - M_r = 5 \log(D) - 5, \quad (7)$$

Equation 5 can be rewritten as

$$r_{RPM} = M_r + 5 \log(v_t) + C, \quad (8)$$

where D is distance in parsec, M_r is the absolute magnitude, and v_t is the heliocentric tangential velocity (the projection of the heliocentric velocity on the plane of the

sky), and C is a constant ($C = -8.25$ if v_t is expressed in $km s^{-1}$). Therefore, for a population of stars with the same v_t , the reduced proper motion is a measure of their absolute magnitude. As shown using similar data as discussed here, halo and disk stars form two well-defined and separated sequences in the reduced proper motion vs. color diagram (e.g., Salim & Gould 2003; Munn et al. 2004; and references therein). We discuss the impact of different metallicity and velocity distributions of halo and disk stars on their reduced proper motion distributions in more detail in Appendix B.

Figure 5 shows reduced proper motion diagrams for stars observed towards the north Galactic pole, constructed for two ranges of observed proper motion: 15-50 $mas yr^{-1}$ and 50-400 $mas yr^{-1}$. The choice of the proper motion range, together with unavoidable apparent magnitude limits, strongly affects the probed distance range: the larger is the proper motion, the closer is the distance range over which the selection fraction is non-negligible. We find that the two sequences closely follow the expectations based on the analysis of metallicity and velocity distributions from I08a. The halo sequence can be efficiently separated by selecting stars with reduced proper motion larger than a boundary generated using the photometric parallax relation from I08a, evaluated for the median halo metallicity ($[Fe/H] = -1.5$) and with $v_t = 180 km s^{-1}$ (see Equation 8). This separation method is conceptually identical to the η separator discussed by Salim & Gould (2003). They also proposed to account for a shift of the reduced proper motion sequences with galactic latitude, an effect which we discuss in more detail in Appendix B. For the reasons described there, to account for the variation of the reduced proper motion sequences away from the Galactic pole, we simply offset the v_t value from 180 $km s^{-1}$ to 110 $km s^{-1}$ (i.e., the separator moves upwards in Figure 5 by 1 mag). While this selection removes some disk binaries, it is designed to exclude most of halo binaries from the sample.

With the aid of reduced proper motion separator, we separate kinematic sample into candidate halo (1,336 pairs) and disk binaries (10,112 pairs). This fraction of halo systems is consistent with the above estimate obtained for the geometric sample. To assess selection effects, we first investigate the sample of single stars. The top left panel in Figure 6 shows the fraction of all the stars shown in Figure 5 that have proper motion larger than 15 $mas yr^{-1}$ and $r < 19.5$ (the latter limit ensures the SDSS-POSS proper motion catalog completeness above $\sim 90\%$). The selection efficiency is a strong function of distance, and falls from its maximum of $\sim 95\%$ for nearby stars to below 50% at a distance of about 1 kpc. The candidate disk stars are detected in significant numbers to ~ 3 kpc, and halo stars beyond ~ 1 kpc. The fraction of selected stars that are classified as halo stars is below 20% closer than ~ 1.5 kpc from the Galactic plane, and becomes essentially 100% beyond 3 kpc.

The kinematic difference between halo and disk stars is blurred at distances beyond 2-3 kpc (see Appendix B), and the majority of disk stars at such distances are misidentified as halo stars (the metallicity distribution implies that disk stars do exist at distances as large as 7 kpc from the Galactic plane, see Figure 10 in I08a). To demonstrate this effect, we use subsamples of candidate

disk and halo binaries identified using the reduced proper motion diagram that have $0.2 < (g-r)_1 < 0.4$. For these pairs it is possible to estimate photometric metallicity (I08a) and use it as an independent population classifier. Figure 7 shows that practically all candidate binaries with $[Fe/H] > -1$ further than ~ 2 kpc from the Galactic plane are misclassified as halo stars when using reduced proper motion diagram.

In summary, geometric sample is heavily dominated by disk binaries, with halo contamination all but negligible closer than about 2 kpc from the plane. Kinematic sample becomes severely incomplete ($< 50\%$) further than ~ 2 kpc from the plane, and has a higher fraction of halo binaries than geometric sample, at a given distance from the plane. However, this halo contamination can be efficiently removed using the reduced proper motion diagram. Unfortunately, the number of selected halo binaries is insufficient in number (1,336 in kinematic and 5,556 in geometric sample), and spans too narrow a color range to robustly constrain the photometric parallax relation. Therefore, both samples of candidate binaries are supposed to yield similar photometric parallax relations, because both are dominated by disk stars.

3. THE PHOTOMETRIC PARALLAX ESTIMATION METHOD

In principle, both the normalization and the shape of the photometric parallax relation (i.e., the shape of the main sequence in the Hertzsprung-Russell diagram) vary as a function of color and metallicity (Laird, Carney & Latham 1988; Siegel et al. 2002). Since our data do not allow a reliable estimate of metallicity over the entire range of observed colors, we can only estimate the “mean” shape of the photometric parallax relation as a function of color, for all metallicities present in the sample. Such a mean shape is approximately an average of individual $[Fe/H]$ -dependent relations, weighted by the sample metallicity distribution. J08 derived such “mean” photometric parallax relations appropriate at the red end for the nearby, metal-rich stars, and at the blue end for distant, metal-poor stars. I08a discuss the offset of photometric parallax relation as a function of metallicity (see their Figure 20), and derived the metallicity range implied by “mean” photometric parallax relations from J08. The derived metallicity range is consistent with the spatial distribution of metallicity derived by I08a and the color-magnitude limits of the SDSS survey.

3.1. The Photometric Parallax Parametrization

We adopt the J08 polynomial $r-i$ parametrization of the photometric parallax relation

$$M_r(r-i|\mathbf{p}) = A+B(r-i)+C(r-i)^2+D(r-i)^3+E(r-i)^4, \quad (9)$$

where $\mathbf{p} = (A, B, C, D, E)$ are the parameters we wish to estimate. To improve their accuracy, Jurić et al. used a maximum likelihood technique to estimate the $r-i$ color from the observed $g-r$ and $r-i$ colors. Because of the brighter flux limit employed here, we use the measured $g-i$ color to derive a best estimate of the $r-i$ color via a stellar locus relation (J08):

$$g-i = 1.39(1-\exp[-4.9(r-i)^3-2.45(r-i)^2-1.68(r-i)-0.050]) + i \quad (10)$$

The $r-i$ color estimate obtained with this method has several times smaller noise than the measured $r-i$ color. This is because the observed dynamic range for the $g-i$ color is much larger than of the $r-i$ color (~ 3 mag vs. ~ 1 mag), while their measurement errors are similar.

3.2. The Parameter Estimation Algorithm

The goal of parameter estimation algorithm is to determine the photometric parallax relation, $M_r(r-i|\mathbf{p})$, that minimizes the width of the distribution of δ values for true binary systems, where $\delta = (M_{r_2} - M_{r_1}) - (r_2 - r_1)$. The χ^2 minimization cannot be used for this purpose because random pairs, if not removed from the sample, will strongly bias the best-fit M_r . The available color, angular separation, and proper motion information are insufficient to separate the random pairs from the true binaries. Therefore, we need to design a fitting algorithm that will be least affected as possible by random pairs.

We begin by studying the behavior of δ values in mock catalogs. The first step in creating a mock catalog is the selection of 51,753 (random) pairs from the random sample. Note that the fraction of true binaries in the random sample is only $\sim 0.25\%$ (see Section 4.1). True binaries are then “created” in the mock catalog by replacing the observed r_2 magnitudes for 20% of pairs with

$$r_2 = r_1 + (M_{r_2} - M_{r_1}) + N(0, 0.1), \quad (11)$$

where $M_r = M_r(r-i|\mathbf{p}_0)$ and $\mathbf{p}_0 = (3.2, 13.30, -11.50, 5.40, -0.70)$ (Equation 2 coefficients from J08). The $N(0, 0.1)$ is a Gaussian random variate added to account for the intrinsic scatter around the photometric parallax relation. The result of this process is a mock sample of candidates where 20% of pairs are “true” binaries, and the rest (80%) is the contamination made of random pairs. The distribution of δ values for “true” binaries is, by definition, a 0.1 mag wide Gaussian centered on zero when $M_r = M_r(r-i|\mathbf{p}_0)$.

Figure 8 (*top*) shows the distribution of δ values for the mock sample evaluated with the “true” $[M_r(r-i|\mathbf{p}_0)]$ photometric parallax relation. The observed δ distribution can be described as a sum of a Gaussian and a non-Gaussian component. The non-Gaussian component is due to random pairs (the contamination), while the Gaussian component (0.1 mag wide and centered on zero) is due to the true binaries.

When an M_r relation different from the “true” (or best-fit) M_r is adopted, the Gaussian component becomes wider and the peak height of the δ distribution decreases, as shown in Figure 8 (*bottom*). At the same time, the peak height of the δ distribution of the contamination changes much less since the distribution is much wider (~ 2.3 mag wide). Therefore, *minimizing* the width of the δ distribution of true binaries, is equivalent to *maximizing* the peak height of the entire δ distribution. We quantify this peak height as the number of candidate binaries in the most populous δ bin.

3.3. The Algorithm Implementation

To robustly explore the parameter space that defines the photometric parallax relation, and to find the best-fit coefficients \mathbf{p} , we implement our algorithm as a Markov chain Monte Carlo (MCMC) process. The MCMC description given here and our implementation of the al-

gorithm are based on examples given by Tegmark et al. (2004), Ford (2005), and Croll (2006).

The basic idea of the MCMC approach is to take an n -step intelligent random walk around the parameter space while recording the point in parameter space for each step. Each successive step is allowed to be some small distance in parameter space from the previous position. A step is always accepted if it improves the fit, and is sometimes accepted on a random basis even if the fit is worse, where the goodness of the fit is quantified by some parameter (usually with χ^2). The random acceptance of a bad fit ensures that the MCMC does not become stuck in a local minimum, and allows the MCMC to fully explore the surrounding parameter space.

We start a Monte Carlo Markov chain by setting all coefficients from Equation 9 to zero ($\mathbf{p}_i = 0$). Using this initial set of coefficients we evaluate $\delta = (M_{r_2} - M_{r_1}) - (r_2 - r_1)$ for all candidate binaries assuming $M_r(r - i | \mathbf{p}_i)$, and bin δ values in 0.1 mag wide bins. The number of candidate binaries in the most populous bin, P_i , is used to quantify the relative goodness of the fit.

Given \mathbf{p}_i , a new candidate step, $\mathbf{p}_n = \mathbf{p}_i + \Delta\mathbf{p}$, is generated, where the step size, $\Delta\mathbf{p}$, is a vector of independent Gaussian random variates with initial widths, σ , set to 1. Using the candidate set of coefficients, \mathbf{p}_n , δ values are evaluated, binned, and the height of the δ distribution is assigned to parameter P_n .

Following the Metropolis-Hastings rule (Metropolis et al. 1953; Hastings 1970) the candidate step is accepted ($\mathbf{p}_{i+1} = \mathbf{p}_n$, $P_{i+1} = P_n$) if $P_n > P_i$ or if $\exp(P_n - P_i) > \xi$, where ξ is a random number between 0 and 1 ($\xi \in [0, 1]$). Otherwise, the candidate step is rejected.

While the Metropolis-Hastings rule guarantees that the chain will converge, it does not specify *when* the convergence is achieved. The speed of the convergence depends on the Gaussian scatter σ used to calculate the step size $\Delta\mathbf{p}$. If the scatter is too large, a large fraction of candidate steps is rejected, causing the chain to converge very slowly. If the scatter is too small, the chain behaves like a random walk, and the number of steps required to traverse some short distance in the parameter space scales as $1/\sigma^2$. The choice of optimal Gaussian scatter σ (for each fitted coefficient), as a function of the position in the parameter space, is not trivial and it can be very complicated even if the fitted coefficients are uncorrelated.

To determine the optimal σ values we follow the Tegmark et al. (2004) prescription (see their Appendix A). After every 100 accepted steps we compute the coefficient covariance matrix $\mathbf{C} = \langle \mathbf{p}\mathbf{p}^t \rangle - \langle \mathbf{p} \rangle \langle \mathbf{p}^t \rangle$ from the chain itself, diagonalize it as $\mathbf{C} = \mathbf{R}\mathbf{\Lambda}\mathbf{R}^t$, and use it to calculate a new step size $\Delta\mathbf{p}' = \mathbf{R}^t \mathbf{\Lambda}^{1/2} \Delta\mathbf{p}$ for each coefficient separately. We find that this transformation greatly accelerates the convergence of a chain.

Due to the stochastic nature of the MCMC, the best-fit relations (coefficients with the highest P_i value in a chain) from different chains will not necessarily be the same. To quantify the intrinsic scatter between different best-fit relations, we run fifty 10,000-element long chains, and select the best-fit coefficients from each chain for subsequent comparison (see Section 3.4). The proper mixing and convergence of chains is confirmed using the

Gelman & Rubin R statistic (Gelman & Rubin 1992). Gelman & Rubin suggest running the chains until $R < 1.2$ for all fitted coefficients. With 10,000 elements in each chain, we obtain $R < 1.01$ for all fitted coefficients.

In the end, we select $\mathbf{p} = (A, B, C, D, E)$ with the highest P_i value among all chains as our best-fit relation. The constant term A is not constrained with our algorithm, because A (from M_{r_2} and M_{r_1}) cancel out when evaluating δ . Instead, we constrain A by requiring $M_r = 10.07$ at $r - i = 1.1$, obtained from trigonometric parallaxes of nearby M dwarfs (West, Walkowicz, & Hawley 2005).

3.4. Algorithm Robustness Test

To test the robustness of our algorithm, we apply it to the mock sample described in Section 3.2. The best-fit relations (obtained from Markov chains) are compared on a $0.1 \leq r - i \leq 1.5$ grid in 0.01 mag steps. We find an rms scatter of 0.05 mag between Markov chains, and 0.05 mag rms scatter between the true and the best-fit relation with the highest P_i value.

We repeat this test with a mock sample containing 30% of true binaries. The rms scatter between the best-fit relations decreases to 0.03 mag, and the rms scatter between the true and the best-fit relation with the highest P_i value decreases to 0.01 mag.

Even when only 20% of sources are true binaries (i.e., contamination by random pairs is 80%) our algorithm recovers the “true” photometric parallax relation at the 0.05 mag (rms) level. The accuracy of the fit increases (to 0.01 mag rms) as the contamination decreases (from 80% to 70%).

3.5. Best-fit Photometric Parallax Relations

We apply the method described in Section 3.3 to two samples of candidate binaries and obtain the best-fit photometric parallax relations

$$M_r = 3.32 + 15.02(r - i) - 18.58(r - i)^2 + 13.28(r - i)^3 - 3.39(r - i)^4 \quad (12)$$

$$M_r = 3.42 + 13.75(r - i) - 15.50(r - i)^2 + 10.40(r - i)^3 - 2.43(r - i)^4 \quad (13)$$

for the geometrically- and kinematically-selected samples, respectively. Candidate halo binaries were removed from the kinematically-selected sample using reduced proper motion diagrams (Section 2.6) before the Equation 13 was derived. The photometric parallax relations for halo stars cannot be robustly constrained using geometrically- or kinematically-selected halo binaries because the color range they span is too narrow ($g - i < 1.0$ at 3-4 kpc, see Figures 4 and 6).

We test the correctness of the shape by studying the dependence of median δ values on the $g - i$ colors of the brighter and the fainter components. If the *shape* of these photometric parallax relations is correct, the distribution of δ values will be centered on zero, and the individual δ values will not correlate with color. The medians are used because they are more robust to outliers (random pairs in the sample). We start by calculating δ values for each candidate binary sample (using the appropriate M_r relation), and then select candidates with $|\delta| < 0.4$. This cut reduces the contamination by random pairs, as demonstrated in Section 3.6. The selected candidate binaries are binned in $g - i$ colors of the brighter and the

fainter component, and the median δ values are shown in Figure 9.

The distributions of the median δ for each pixel are fairly narrow (0.07 mag), and centered on zero. Irrespective of color and the choice of the two best-fit photometric parallax relations, the deviations are confined to the 0.25 mag range, placing an upper limit on the errors in the mean shape of the adopted relations.

In Figure 10 we compare the adopted photometric parallax relations to J08 “faint”

$$M_r = 4.0 + 11.86(r-i) - 10.74(r-i)^2 + 5.99(r-i)^3 - 1.20(r-i)^4 \quad (14)$$

and “bright”

$$M_r = 3.2 + 13.30(r-i) - 11.50(r-i)^2 + 5.40(r-i)^3 - 0.70(r-i)^4 \quad (15)$$

photometric parallax relations. The rms difference between Equations 12 and 13, and Equation 15 is ~ 0.13 mag, comparable to the rms difference between our Equations 12 and 13 (~ 0.13 mag). The maximum difference between Equations 12 and 13, and Equation 15 is ~ 0.25 mag, again comparable to the maximum difference between our Equations 12 and 13 (~ 0.25 mag). The different color distributions of the two samples, shown in Figure 11, together with metallicity effects, is the most likely explanation for differences between the two photometric parallax relations.

3.6. The Analysis of the Scatter in Predicted Absolute Magnitudes

The scatter in δ values can be expressed as

$$\langle \delta^2 \rangle = \langle (\Delta M - \Delta m)^2 \rangle \approx \langle \Delta M^2 \rangle + \langle \Delta r^2 \rangle, \quad (16)$$

where $\langle \Delta M^2 \rangle$ is the scatter in predicted absolute magnitudes, and $\langle \Delta m^2 \rangle$ is the scatter in measured apparent magnitudes. Since the photometric uncertainties of SDSS are well understood, the intrinsic scatter around the $M_r(r-i)$ relation is possible to measure and characterize.

In Figure 12 we plot the observed distributions of δ values for the geometrically- and kinematically-selected binaries, and overplot the δ distribution of the random sample. The δ values for the random sample were calculated with Equations 12 and 13, respectively. The δ distribution of the random sample was fitted to the observed δ distribution in the $|\delta| > 1$ range using the Kolmogorov-Smirnov test.

By comparing the random and the observed δ distributions, we find that the two match well for $|\delta| > 1$ (the Kolmogorov-Smirnov test reports $P \sim 0.95$), indicating that candidate binaries with $|\delta| > 1$ are almost certainly random pairs. On the other hand, as δ approaches zero, the two distributions become remarkably different ($P \sim 10^{-7}$ for $|\delta| < 1$), indicating that these candidate binaries are dominated by true binary systems, and not by random pairs.

The δ distribution for true binaries (Figure 12, dashed line), obtained by subtracting the random from the observed δ distribution, is clearly not Gaussian. It can be modeled as a sum of two Gaussian distributions (“narrow” and “wide”) centered close to zero, and about 0.1 mag and 0.55 mag wide. The centers, widths, and areas for the best-fit Gaussian distributions are given in

Table 1.

To determine the consistency of the observed scatter with photometric errors, we normalize the δ values for the kinematically-selected sample with expected formal errors,

$$\sigma_\delta = (\sigma_{M_{r_2}}^2 + \sigma_{M_{r_1}}^2 + \sigma_{r_2}^2 + \sigma_{r_1}^2)^{1/2}, \quad (17)$$

and plot the δ/σ_δ distribution in Figure 13. The δ/σ_δ distribution for true binaries is not a Gaussian with a width of 1, as we would expect if the scatter in the δ distribution was only due to photometric errors in the gri bands (note that the expected random error in M_r is about 5-10 times larger than the random error of the $g-i$ color because $dM_r/d(g-i)$ varies from ~ 10 at the blue edge to ~ 5 at the red edge).

The width of δ/σ_δ distribution for the geometrically-selected candidate binaries is about 3 times smaller than in the kinematically-selected sample. We find that this is due to *overestimated* photometric errors in the geometrically-selected sample, as shown in Figure 14. The overestimated photometric errors in the gri bands overestimate the expected formal error σ_δ , and the overall δ/σ_δ distribution is too narrow. We speculate that the small angular separation ($\sim 3''$) between the components is the cause of overestimated photometric errors (perhaps due to sky background estimates). The small angular separation of components does not affect the magnitudes of stars in the geometrically-selected sample. If it did, the two δ distributions would be significantly different which, as shown in Figure 12, is not the case.

The observed non-Gaussian scatter in predicted absolute magnitudes may be due to photometric parallax variation as a function of metallicity. As noted at the beginning of Section 3, we can only estimate the “mean” shape of the photometric parallax relation. Since the intrinsic photometric parallax for a given wide binary system is different from the mean relation, ΔM (the difference of predicted absolute magnitudes) and Δm (the measured difference of apparent magnitudes) will differ. This discrepancy will increase for systems where the components have significantly different colors.

To test the assumption that the shape of photometric parallax relation increases the scatter in predicted absolute magnitudes, we use the mock sample constructed in Section 3.2 and add a color-dependent offset to apparent magnitudes

$$r'_1 = r_1 + \xi(g-i)_1 \quad (18)$$

$$r'_2 = r_2 + \xi(g-i)_2 \quad (19)$$

where ξ is a random number between zero and one (the same for both components). These color-dependent offsets simulate the change in the shape of the photometric parallax relation due to metallicity. We apply the algorithm described in Section 3.3 to the mock sample, and obtain a revised photometric parallax relation. Using this relation, we analyze the distribution of δ values and find that it can be modeled as a sum of two Gaussians centered on zero, with widths of 0.1 and 0.3 mag. This result suggests that the non-Gaussian scatter observed in candidate samples may be caused by the difference between the shapes of the mean photometric parallax relation and a true relation for a given metallicity (and perhaps other effects, such as age).

This model-based conclusion is consistent with a direct comparison of relations derived here and the relations from I08a evaluated for the median halo metallicity ($[Fe/H] = -1.5$) and the median disk metallicity ($[Fe/H] = -0.7$ for distances probed by our sample; see Figure 5 in the above paper). The two relations corresponding to halo and disk stars are offset by 0.6 mag due to metallicity difference. Our relations match the low-metallicity relation at the blue end and the high-metallicity relation at the red end. Therefore, in the worst case scenario of extremely blue ($r - i = 0.3$) and red ($r - i = 1.4$) disk stars, the maximum error in the difference of their absolute magnitudes is 0.6 mag. When convolved with the observed color distribution of pairs, the expected scatter is about 0.2-0.3 mag, consistent with the observed and simulated widths of the δ distributions.

Unresolved binarity of components in candidate samples may also contribute to the non-Gaussian scatter in predicted absolute magnitudes. The multiplicity studies of G dwarfs (Duquennoy & Mayor 1991) and M dwarfs (Fischer & Marcy 1992) find that a significant fraction of G and M dwarf stars (40 – 60%) are unresolved binary systems. If a component of a wide binary system is an unresolved binary system, its luminosity will be underestimated (with the magnitude of the offset depending on the actual composition of the binary) and the δ value for the wide binary system will systematically deviate from zero. In Appendix C we model the presence of unresolved binaries in wide binary systems, and find that the model can explain the observed δ scatter.

Therefore, both the intrinsic variations of the photometric parallax relation and unresolved binaries can explain the observed non-Gaussian scatter of δ . The data discussed here are insufficient to disentangle these two effects.

Finally, the uncertainty in predicted absolute magnitudes (error distribution for photometric parallax method) can be obtained by drawing random values, x , from a non-Gaussian distribution

$$f(x) = A_1 N(x|\mu_1, \sigma_1/\sqrt{2}) + A_2 N(x|\mu_2, \sigma_2/\sqrt{2}), \quad (20)$$

where $N(x|\mu, \sigma)$ are Gaussian distributions, and the best-fit parameters are listed in Table 1.

4. THE PROPERTIES OF WIDE BINARIES

The best-fit photometric parallax relation can be utilized to further refine the samples of candidate binaries and to address questions about their dynamical and physical properties such as

- Do wide binaries have the same spatial distribution as single stars?
- Do wide binaries have the same color distribution as single stars?
- Are the color distributions of components in wide binary systems consistent with random pairings?
- What is the distribution of semi-major axis for wide binaries?
- Does the distribution of semi-major axis vary with the position in the Galaxy?

4.1. High-Efficiency Samples of Candidate Binaries

We use the best-fit photometric parallax relations to select samples of candidate binaries with high selection efficiency (high fraction of true binaries) by imposing further constraints on δ values in geometric and kinematic sample.

As shown in Figure 12, the fraction of random pairs in the candidate sample is simply $A_{random}/A_{observed}$, where A_{random} and $A_{observed}$ are the integrals of the random (triangles) and total (thick solid line) δ distributions. The fraction of true binaries, or the *selection efficiency*, is then

$$\epsilon = 1 - A_{random}/A_{observed} \quad (21)$$

Without a cut on δ , the fraction of true binaries (the selection efficiency) in the geometrically- and kinematically-selected samples is 34% and 35%, respectively. It is reassuring to find that the ϵ value for the geometrically-selected sample obtained here, and the one measured in Section 2.3 match so well (at a 1% level), even though the two methods for estimating ϵ are independent.

The selection efficiency of 35% for the kinematically-selected sample may seem low, given that only 0.5% of random pairs pass the common proper motion criteria. This points to a low fraction of true binaries with angular separation greater than $15''$. If this fraction is about 1/400 (0.25%), the common proper motion criteria will select 2 random pairs (0.5% out of a 400), and only 1 true binary system. Therefore, 66% of the sample (2 out of 3) will be random pairs, and 34% (1 out of 3) will be true binary systems, similar to what we find for the kinematically-selected sample. The result that only 1/400 pairs with $\theta > 15''$ are true binaries puts the fraction of random pairs in the random sample at 99.75%.

Figure 12 shows that the true binaries have a much smaller range of δ values than the random pairs. Therefore, a cut on δ would reduce the contamination, and increase the fraction of true binaries in a sample. By requiring $|\delta| < 0.4$, we construct samples where 63% and 64% of candidates are true binaries. The numbers of candidate binaries in these cleaner samples are 16,575 (geometrically-selected) and 5,157 candidates (kinematically-selected), with the expected total number of true binaries about 13,743. The sample efficiency for the geometric sample can be further increased to 90% by requiring $|\delta| < 0.2$ and $Z < 0.3$ kpc, where Z is the height above the Galactic plane. Compared to the existing catalogs of wide binaries by Chanamé & Gould (2004) and Lépine & Bongiorno (2007), our samples represent a 20-fold increase in the number of candidate binaries and probe much deeper into the halo (to ~ 4 kpc). Although a non-negligible fraction of candidate pairs are due to random pairings ($\sim 35\%$), the increase in the number of potential physical pairs is substantial.

We emphasize that our method only selects candidates where both components are *main-sequence* stars, while rejecting systems where one of the components has evolved off the main sequence. This is due to the photometric parallax relation, as defined here, being correct for main-sequence stars only. Together with the small expected fraction of giant stars in our sample due to faint apparent magnitudes (1-2%, Finlator et al. 2000; I08a), this bias results in practically pure main-sequence sam-

ple. We note that the application of a photometric parallax relation that corresponds to some mean metallicity distribution introduces systematic errors in estimated M_r . We partially mitigate this problem by averaging distances determined for each binary component (using Equation 12). Based on the behavior of photometric parallax relations and δ distribution discussed in Section 3.6, the systematic uncertainty in obtained distances is most likely not larger than 10-15% (an underestimate due to faint bias for blue stars). Another source of overall systematic uncertainty in distances is the normalization of Equation 12 adopted from West, Walkowicz, & Hawley (2005). This normalization corresponds to nearby (<100 pc) metal-rich stars, while most stars in our sample are distances of the order 1 kpc. The disk metallicity gradient discussed by I08a implies systematic distance overestimate of about 10-20%, partially cancelling the above underestimate. These systematic uncertainties propagate as systematic uncertainties of derived semi-major axes discussed in Section 4.3.

4.2. The Color Distribution of Wide Binaries

The luminosity of a main-sequence star, and thus its color via photometric parallax relation, can be used as a proxy for stellar mass. The color-color distribution of wide binaries, therefore, provides constraints on the distribution of stellar masses in wide binary systems. To find the color distribution of wide binaries, we select a volume-complete ($0.7 < d/kpc < 1.0$) subsample of geometrically-selected candidate binaries with $|\delta| < 0.4$, and plot their distribution in the $(g-i)_2$ vs. $(g-i)_1$ color-color diagram in Figure 15 (*top*). The sample is complete in the $0.4 < g-i < 2.8$ color and $4,200 \text{ AU} < a < 10,000 \text{ AU}$ semi-major axis range (see Section 4.3). Even though the $|\delta| < 0.4$ cut increases the fraction of true binaries, about 14% of candidates (in the $0.7 < d/kpc < 1.0$ range) are still random pairs that contaminate the map. To remove the contamination, first we select pairs from the random sample (see the end of Section 2.2) with $|\delta| < 0.4$ and $0.7 < d/kpc < 1.0$. The $|\delta| < 0.4$ cut on the random sample will not increase the fraction of true binaries (ϵ) above $\sim 1\%$ because ϵ decreases rapidly with θ (see Figure 21 (*middle left*) in Section 4.3), and the pairs in the random sample have $\theta > 20''$. The $(g-i)_2$ vs. $(g-i)_1$ distribution of this random sample is shown in Figure 15 (*middle*). The maps are essentially probability density maps as pixels sum to 1. To correct for the contamination in the top map, we multiply each pixel in the random map with 0.14 (that being the contamination in the candidate binary sample), and subtract two maps. The corrected map, presented in Figure 15 (*bottom*), shows that the color-color distribution of true binary systems is fairly uniform, has a local maximum around $(g-i)_{1,2} \sim 2.5$, and reflects the underlying luminosity function which peaks for red stars (c.f. Figure 4).

The map shown in Figure 15 (*bottom*) describes the probability density, $P[(g-i)_1, (g-i)_2]$, of a wide binary system with components that have $(g-i)_1$ and $(g-i)_2$ colors falling into a given pixel. This probability density can be expressed as a product

$$P[(g-i)_1, (g-i)_2] = P[(g-i)_B|(g-i)_A] P[(g-i)_A] \quad (22)$$

where $P[(g-i)_B|(g-i)_A]$ is the conditional probability density of having one component with $(g-i)_B$ color

in a wide binary system where the other component has $(g-i)_A$, and $P[(g-i)_A]$ is the probability density that a star with $g-i = (g-i)_A$ color is in a wide binary system. These probability densities may also vary with Galactic coordinates (e.g., with the height above the Galactic plane), but we cannot study such effects directly because the samples are volume-complete only in the $0.7 < d/kpc < 1.0$ range.

The conditional probability density, $P[(g-i)_B|(g-i)_A]$, can be extracted from Figure 15 (*bottom*) map by selecting pixels where either $(g-i)_1 = (g-i)_A$, or $(g-i)_2 = (g-i)_A$. The resulting $P[(g-i)_B|(g-i)_A]$ for several values of $(g-i)_A$ are shown in Figure 16. Red stars ($(g-i)_A \gtrsim 2.0$) are more likely to be associated with another red star than with a blue star, while for blue stars the companion color distribution is flat. The best-fit analytic functions that describe the observed trends are given in Table 2.

The probability density, $P[(g-i)_A]$, that a star with $g-i = (g-i)_A$ is in a wide binary system can be derived by comparing the $g-i$ color distribution of stars in wide binary systems with the $g-i$ color distribution of all the stars in the same volume. As shown in Figure 17 (*top*), the $g-i$ color distribution of stars in the volume-complete wide binary sample roughly follows the $g-i$ color distribution of all the stars in the same volume. The ratio of the two distributions (renormalized to an area of 1) gives the $P[(g-i)_A]$, and is shown in the bottom panel.

The probability for a star to be in a wide binary system ($P[(g-i)_A]$) is independent of its color. Given this color, the companions of red components seem to be drawn randomly from the stellar luminosity function, while blue components have a larger blue-to-red companion ratio than expected from luminosity function. These results are consistent with recent results by Lépine & Bongiorno (2007). The overall fraction of stars in wide binary systems is discussed in the next section.

4.3. The Spatial Distribution of Wide Binaries

If the semi-major axis distribution function, $f(a)$, is known, the number of stars in wide binary systems can be determined by integrating $f(a)$ from some lower cut-off, a_1 , to the maximum semi-major axis, a_2 . The power-law frequency distribution, $f(a) \propto a^\beta$, $\beta = -1$, is known in the context of wide binaries as the Öpik distribution (OD; Öpik 1924). When semi-major axis distribution of wide binaries follows the OD, the frequency distribution of $\log(a)$ is a straight line with a slope of zero (Poveda, Allen & Hernández-Alcántara 2007). Alternatively, an equivalent representation of OD is the cumulative distribution $N[<\log(a)] \propto \log(a)$. In this form, OD is a straight line with a positive slope. We use the cumulative representation, instead of differential, because it reduces the counting noise in sparsely populated bins (though the errors become correlated between bins).

We utilize geometrically-selected candidate binaries (see Section 4.4 for a discussion of the kinematic sample), but do not limit the selection to $\theta < 4''$, as we did in Section 2.3. Since $a \propto \theta$, the removal of upper limit on θ allows us to probe an extended range of semi-major axes. The downside is that random pairs dominate at large θ and a careful accounting for contamina-

tion as a function of θ is required before the the $f(a)$ distribution can be constrained. Since we only know the projected separation of our pairs, we use a statistical relation to calculate the average semi-major axis, $\langle a \rangle$, as $\langle a \rangle = 1.411 \theta d$, where d is the heliocentric distance (Couteau 1960). Hereafter, we drop the brackets and simply note the average semi-major axis as a .

Figure 18 (*top left*) shows the cumulative distribution of $\log(a)$ for candidate wide binaries with $|\delta| < 0.2$ selected from the $0.7 < Z/kpc < 1.0$ range. The cumulative distribution does not follow a straight line, as predicted by the OD, but actually increases its slope with $\log(a)$. We assume that this is due to an increasing fraction of random pairs at high $\log(a)$, and proceed to verify this assumption.

Figure 18 (*top right*) shows the differential distribution of angular separation for the selected sample. For $\theta > \theta_{max}$ the observed and random distributions closely match, demonstrating that random pairs dominate at high θ (or high $\log(a)$). To calculate how the fraction of true binaries (or random pairs) changes as a function of θ , we fit $f_{rnd}(\theta) = C\theta$ to the observed histogram, and calculate the fraction of true binaries, ϵ , using Equation 2 (see Section 2.3). The calculated ϵ values, as well as the best-fit second-degree polynomial, $\epsilon(\theta)$, are shown in Figure 18 (*middle left*). As an independent test, the selection efficiency was calculated using Equation 21 (i.e., from the δ distribution) for three θ -selected subsamples, and the obtained values agree with $\epsilon(\theta)$ at a level of 1%. The angular separation for which ϵ falls below $\sim 5\%$ is defined as θ_{max} . The fraction of true binaries ($\epsilon(\theta)$) also changes as a function of Z , and is determined separately for different distance bins.

Since the candidates are restricted in Z ($Z_{min} = 0.7$ kpc to $Z_{max} = 1.0$ kpc in this example) and θ ($3''$ to θ_{max}), to ensure a uniform selection in the Z vs. a space we define

$$a_{min} = 3'' \cdot 1.411 \cdot 1000 Z_{max} \quad (23)$$

and

$$a_{max} = \theta_{max} \cdot 1.411 \cdot 1000 Z_{min} / \sin(45^\circ) \quad (24)$$

as the minimum and maximum probed semi-major axis, shown as the selection box in Figure 18 (*middle right*). The $\sin(45^\circ)$ factor is to account for the fact that the candidates are restricted to high ($b > 45^\circ$) Galactic latitudes.

To correct the cumulative distribution of $\log(a)$, we assign a probability $\epsilon(\theta)$ to each candidate binary in the a_{min} to a_{max} range, and add the probabilities (instead of counting candidates) when making the cumulative $\log(a)$ distribution. The corrected cumulative distribution, shown in Figure 18 (*bottom left*), follows a straight line up to the turnover point, a_{break} . We define a_{break} as the average semi-major axis for which the straight line fit to the cumulative distribution deviates by more than 1.5%. In addition to a_{break} , we also measure the slope of the cumulative distribution where it follows the straight line. It can be shown that the slope of the cumulative distribution is equal to the constant of proportionality, N_0 , in Öpik distribution, $f(a) = N_0/a$. The number of binaries can be calculated by integrating $f(a)$ from a_1 to a_2 , and we obtain $N_{bin} = N_0 \log(a_2/a_1)$. For inte-

gration limits we choose $a_2 = a_{break}$ where we assume that systems with semi-major axes greater than a_{break} are no longer bound, and $a_1 = 100$ AU (since $a_2 \gg a_1$, the results are not very sensitive to the choice of a_1).

The uncertainty in a_{break} , shape of $f(a)$ (or power-law index β), and number of binaries (N_{bin}) are estimated using Monte Carlo simulations. We find that the uncertainty in a_{break} is less than 0.1 dex, and the error on the power-law index (β) is $\lesssim 0.1$. The uncertainty in measuring N_{bin} is about 10%. The corrected cumulative $\log(a)$ distribution obtained from one of these simulations is shown in Figure 18 (*bottom right*). The semi-major axis distribution of “true” binaries in the simulation sample is $f(a) \propto a^{-0.8}$, and is valid between 100 AU and $a_{break} = 10,000$ AU. The turnover in the distribution happens because there are no “true” binaries above 10,000 AU, only random pairs, similar to what we observe in real data. This similarity is a strong warning not to over-interpret the slope of $f(a)$ beyond a_{break} .

To estimate the dependence of β (shape of $f(a)$), a_{break} , and N_0 on color, we divide the $0.7 < Z/kpc < 1.0$ sample into three color subsamples using $(g-i)_1 = 1.8$ and $(g-i)_2 = 1.5$ lines. We find that $f(a)$ follows OD in all three subsamples ($\beta = -1$), and that the average a_{break} is 3.99, with a 0.07 root-mean-square scatter. The a_{break} for the full $0.7 < Z/kpc < 1.0$ sample is 4.02. These results suggest that a_{break} and the shape of $f(a)$ are *independent of color of binaries*. The N_0 value, and subsequently the number of binaries, will depend on the sample’s color range. For the full $0.7 < Z/kpc < 1.0$ sample, the number of binaries is

$$N_{bin} = (N_0^1 + N_0^2 + N_0^3) \log_{10}(a_2/a_1), \quad (25)$$

where N_0^i , $i = 1, 2, 3$, are N_0 values measured for each color subsample. Therefore, the number of binaries calculated for a distance bin will change as the color range changes. Assuming that the $g-i$ color distribution of binaries does not change with Z , we can use the $g-i$ color distribution for the $0.7 < Z/kpc < 1.0$ sample (solid line in Figure 17 (*top*)), to correct for color incompleteness. We also assume that the fraction of binaries outside the $0.4 < g-i < 2.8$ color range is small. The correct number of binaries is then

$$N_{bin} = N_0/A[(g-i)_{min}, (g-i)_{max}] \log_{10}(a_2/a_1), \quad (26)$$

where $A[(g-i)_{min}, (g-i)_{max}]$ is the area underneath the solid line histogram in Figure 17 (*top*), between $(g-i)_{min}$ and $(g-i)_{max}$ ($g-i$ color range for a given distance bin).

The estimated systematic error in a_{break} due to the choice of the $|\delta|$ cut is measured using $|\delta| < 0.1$ and $|\delta| < 0.4$ samples. We find that a_{break} changes by $\lesssim 0.03$ dex between these samples. This result suggests that a_{break} is not sensitive to the choice of the $|\delta|$ cut. Similarly, the change in a_{break} is less than 0.03 dex if the estimate of $\epsilon(\theta)$ is off by ± 0.1 ($\sim 10\%$ change) from the best-fit $\epsilon(\theta)$.

To establish whether semi-major axis distribution follows the OD in other Z bins, we repeat the $f(a)$ and a_{break} measuring procedure on 8 Z bins, and show the corrected cumulative distributions with best-fit straight lines in Figure 19. In general, the corrected cumulative distributions follow a straight line, and then start to deviate from it at a_{break} . In the $0.1 < Z/kpc < 0.4$ bin we do not see a turnover due to a narrow range of probed

projected separations ($\theta_{max} = 16''$ limits the range to 3193 AU, see Figure 20), and only determine the upper limit on a_{break} .

As the average height above the Galactic plane increases, the a_{break} moves to higher values. We investigate this correlation in more detail in Figure 21 (*top left*). The data follow a straight line $\log(a_{break}) = k \log(Z[pc]) + l$, where $k = 0.72 \pm 0.05$ and $l = 1.93 \pm 0.15$, or approximately, $a_{break}[AU] = 12,300 Z[kpc]^{0.7}$ in the $0.3 < Z/kpc < 3.0$ range.

It is possible that a_{break} also depends on the cylindrical radius, R , with the Sun at $R_{\odot} = 8$ kpc, and perhaps on the local density of stars, ρ . Because the sample is dominated by stars at high Galactic latitudes, it is hard to disentangle the Z dependence from the other two effects (the R range is small, and ρ varies strongly with Z). We attempt to do so using the volume-complete $0.7 < Z/kpc < 1.0$ sample. First we divide this sample into three subsamples with median Galactic latitudes, $\langle b \rangle$, of 35° , 49° , and 80° and determine a_{break} for each subsample. The best-fit a_{break} varies by ~ 0.3 dex between the low-latitude and high-latitude subsample, despite the same median Z . When the $0.7 < Z/kpc < 1.0$ sample is divided into the Galactic anticenter ($90^\circ < l < 270^\circ$) and the Galactic center ($l > 270^\circ$ or $l < 90^\circ$) subsamples, the best-fit a_{break} varies by ~ 0.1 dex. These variations suggest that the best-fit Z dependence does not fully capture the behavior of a_{break} . Nevertheless, they are smaller ($\lesssim 0.3$ dex) than the observed variation of a_{break} (~ 1 dex).

The spatial distribution of wide binaries can now be compared to the number density of all stars as a function of height above the Galactic plane. In Figure 21 (*bottom left*) we show that wide binaries closely follow the spatial distribution of stars, with exponential decline in the number density as a function of Z . The fraction of binaries relative to the number of all stars, shown in the bottom right panel, changes by only a factor of 2 over a range of 3 kpc, starting from 0.9% at $Z = 500$ pc and declining to 0.5% at $Z = 3000$ pc.

4.4. The Limitations of the Kinematic Sample

It would be informative to repeat the $f(a)$ and a_{break} analysis using kinematically-selected binaries, but unfortunately, the apparent incompleteness of SDSS-POSS proper motion data at $\theta < 9''$ prevents us in doing so. As shown in Figure 22, the number of common proper motion pairs drops sharply below $\theta = 9''$, probably due to blending of close sources in the POSS data. Because of this θ cut-off, for the same range in Z , the effective a_{min} for the kinematic sample is three times that of the geometric sample (where the lower limit on θ is $3''$). In the case of $0.1 < Z/kpc < 0.4$ sample observed here, the smallest probed semi-major axis (a_{min}) is at 5079 AU, well above the a_{break} value of 4534 AU predicted by the $a_{break} \propto Z^{0.7}$ relation. Since we are outside the range where OD is valid, we cannot measure where the turnover in $f(a)$ happens, and cannot determine a_{break} or N_{bin} . In all the other Z bins, a_{min} is also above the predicted a_{break} value, and therefore outside the Öpik regime.

5. DISCUSSION AND CONCLUSIONS

We have presented a novel approach to photometric parallax estimation based on samples of candidate

wide binaries selected from the Sloan Digital Sky Survey (SDSS) imaging catalog. Our approach uses the fact that binary system's components are at equal distances and estimates the photometric parallax relation for main-sequence stars by minimizing the difference of their distance moduli. While this method is similar to constraints on photometric parallax relation obtained from globular clusters in that it does not require absolute distance estimates, it has the advantage that it extends to redder colors than available for globular clusters observed by the SDSS, and it implicitly accounts for the metallicity effects.

The derived best-fit photometric parallax relations represent metallicity-averaged relations and thus provide an independent confirmation of relations proposed by J08 in their study of the Galactic structure. An important result of this work is our estimate of the expected error distribution for absolute magnitudes determined from photometric parallax relations (a root-mean-square scatter of ~ 0.3 mag, see Section 3.6), which is in good agreement with modeling assumptions adopted by J08. The mildly non-Gaussian error distribution is consistent with both the impact of unresolved binary stars, and the variation of photometric parallax relation with metallicity; we are unable to disentangle these two effects.

The best-fit photometric parallax relations enabled the selection of high-efficiency samples of disk wide binaries with $\sim 22,000$ candidates, that include about 14,000 true binary systems (efficiency of $\sim 2/3$). Using the photometric measurements and angular distance of the two components, samples with efficiency exceeding 80% can be constructed (see Section 4.1). Such samples could be used as a starting point to further increase the selection efficiency with the aid of radial velocity measurements. Spectral observations of systems where the brighter component is an F/G star, for which it is easy to estimate metallicity, could be used to calibrate both spectroscopic and photometric methods for estimating metallicity of cooler K and M dwarfs. Compared to the state-of-the-art catalogs of wide binaries by Chanamé & Gould (2004) and Lépine & Bongiorno (2007), the samples discussed here represent a significant increase in the number of potential binaries, and probe larger distances (to ~ 4 kpc). To facilitate further studies of wide binaries, we make the catalog publicly available⁹.

Using the high-efficiency subsamples, we analyzed their dynamical and physical properties. We find that the spatial distribution of wide binaries follows the distribution of single stars to within a factor of 2, and that the probability for a star to be in a wide binary system is independent of its color. However, given this color, the companions of red components seem to be drawn randomly from the stellar luminosity function, while blue components have a larger blue-to-red companion ratio than expected from luminosity function (see Section 4.2). These results are consistent with recent results by Lépine & Bongiorno (2007), and provide strong constraints for the scenarios describing the formation of such systems (e.g., Giersz 2006 and references therein; Clarke 2007; Hurley, Aarseth & Shara 2007).

We also study the semi-major axis distribution of wide

⁹ The catalog can be downloaded from [HREF]http://www.astro.washington.edu/besar/SDSS_wide_binaries.tar.gz

binaries in the 2,000–47,000 AU range (see Section 4.3). The observed distribution is well described by the Öpik distribution, $f(a) \propto 1/a$, for $a < a_{break}$, where a_{break} increases roughly linearly with the height above the Galactic plane ($a_{break} \sim 12,300$ AU at $Z = 1$ kpc). Alternatively, the a_{break} correlates with the local number density of stars as $a_{break} \propto \rho^{-1/4}$, but we are unable to robustly identify the dominant correlation (Z and ρ are highly correlated).

The distribution of semi-major axes for wide binaries was also discussed by Chanamé & Gould (2004). They used a sample of wide binaries selected using common proper motion from the rNLTT catalog (Gould & Salim 2003), and found $f(a) \propto 1/a^{1.6}$, with no evidence of a turnover at $a \lesssim 3000$. Their sample extended to larger angular separations than ours, and probed smaller distances. On the other hand, Poveda, Allen & Hernández-Alcántara (2007) used wide binaries from the same Chanamé & Gould (2004) sample, and detected Öpik distribution, $f(a) \propto 1/a$, for $a < 3,000$, consistent with the result of Chanamé & Gould (2004). In a recent study, Lépine & Bongiorno searched for faint common proper motion companions of Hipparcos stars and detected a turnover from Öpik distribution to a steeper distribution around $a \sim 3,000$ AU. Their sample also probed much smaller distances than ours. We compare these results in Figure 23. As evident, the variation of a_{break} with distance from the Galactic plane detected here (approximately with distance, as shown in Figure 23, since stars in our sample are mostly at high galactic latitudes), is consistent with the above results that are based on more local samples. In particular, this comparison of different studies suggests that the flattening of $f(a)$ for small a that “puzzled” Chanamé & Gould (see their section 4.3) is probably due to a combination of selection effects and the approach of the domain where Öpik distribution is valid in their sample.

The Öpik distribution suggests that the process of star formation produces multiple stars, which evolve towards binaries after ejecting one or more single stars (Poveda, Allen & Hernández-Alcántara 2007). The departure from the Öpik distribution may be evidence for disruption of wide binaries over long periods of time by passing stars, giant molecular clouds, massive compact halo objects (MACHOs), or disk and Galactic tides (Heggie 1975; Weinberg, Shapiro & Wasserman 1987; Yoo, Chanamé, & Gould 2004). However, we note that the $a_{break} \propto \rho^{-1/4}$ correlation (see Figure 21) is outside the expected range discussed by Yoo, Chanamé, & Gould (2004) ($a_{break} \propto \rho^{-2/3}$ for close strong encounters, and $a_{break} \propto \rho^{-1}$ for weak encounters).

The samples presented here can be further refined and enlarged. First, the SDSS covers only a quarter of the sky. Upcoming next-generation surveys, such as the SkyMapper (Keller et al. 2007), the Dark Energy Survey (Flaugher et al. 2007), Pan-STARRS (Kaiser et al. 2002) and the Large Synoptic Survey Telescope (Ivezić et al. 2008b, LSST hereafter), will enable

the construction of such samples over most of the sky. Due to fainter flux limits (especially for the Pan-STARRS and LSST), the samples will probe a larger distance range and will reach the halo-dominated parts of the Galaxy. Furthermore, due to improved photometry and seeing (e.g., for the LSST, by about a factor of two), the selection will be more robust. We scale the 20,000 candidates discussed here, assuming $\log(N) = C + 0.4r$, to the LSST depth that enables accurate photometric metallicity ($r < 23$; I08a) and predict a minimum sample size of $\sim 400,000$ candidate wide binary systems in 20,000 deg² of sky. It is likely that the sample would include more than a million systems due to the increase of the stellar counts close to the Galactic plane.

Another important development will come from the Gaia mission (Perryman et al. 2001; Wilkinson et al. 2005), which will provide direct trigonometric distances for stars with $r < 20$. With trigonometric distances, accurate photometric parallax relation can be used to provide strong constraints on the incidence and color distribution of unresolved multiple systems. Until then, a radial velocity survey of candidate binaries assembled here could help with pruning the sample from random associations, and with better characterization of various selection effects.

This work was supported by the NSF grant AST-0707901, and the NSF grant AST-0551161 to the LSST for design and development activity. M. J. gratefully acknowledges support from the Taplin Fellowship and from the NSF grant PHY-0503584. We are grateful to Nick Cowan and Eric Agol (UW) for help with the Markov chain Monte Carlo code. Early motivation for this analysis came from a preliminary study by Taka Sumi.

Funding for the SDSS and SDSS-II has been provided by the Alfred P. Sloan Foundation, the Participating Institutions, the National Science Foundation, the U.S. Department of Energy, the National Aeronautics and Space Administration, the Japanese Monbukagakusho, the Max Planck Society, and the Higher Education Funding Council for England. The SDSS Web Site is <http://www.sdss.org/>.

The SDSS is managed by the Astrophysical Research Consortium for the Participating Institutions. The Participating Institutions are the American Museum of Natural History, Astrophysical Institute Potsdam, University of Basel, University of Cambridge, Case Western Reserve University, University of Chicago, Drexel University, Fermilab, the Institute for Advanced Study, the Japan Participation Group, Johns Hopkins University, the Joint Institute for Nuclear Astrophysics, the Kavli Institute for Particle Astrophysics and Cosmology, the Korean Scientist Group, the Chinese Academy of Sciences (LAMOST), Los Alamos National Laboratory, the Max-Planck-Institute for Astronomy (MPIA), the Max-Planck-Institute for Astrophysics (MPA), New Mexico State University, Ohio State University, University of Pittsburgh, University of Portsmouth, Princeton University, the United States Naval Observatory, and the University of Washington.

APPENDIX
A. SQL QUERIES

The following SQL queries were used to select initial samples of candidate binaries through the SDSS CasJobs interface. When running these queries, the database context must be set to “DR6” or higher.

```

select -- geometric selection of candidate binaries

round(p1.ra,6) as ra1, round(p1.dec,6) as dec1, round(p1.extinction_r,3) as rExt1,
round(p1.psfMag_u,3) as psf_u1, round(p1.psfMag_g,3) as psf_g1,
round(p1.psfMag_r,3) as psf_r1, round(p1.psfMag_i,3) as psf_i1,
round(p1.psfMag_z,3) as psf_z1, round(p1.psfMagErr_u,3) as psfErr_u1,
round(p1.psfMagErr_g,3) as psfErr_g1, round(p1.psfMagErr_r,3) as psfErr_r1,
round(p1.psfMagErr_i,3) as psfErr_i1, round(p1.psfMagErr_z,3) as psfErr_z1,
p1.objid as objid1,

round(p2.ra,6) as ra2, round(p2.dec,6) as dec2, round(p2.extinction_r,3) as rExt2,
round(p2.psfMag_u,3) as psf_u2, round(p2.psfMag_g,3) as psf_g2,
round(p2.psfMag_r,3) as psf_r2, round(p2.psfMag_i,3) as psf_i2,
round(p2.psfMag_z,3) as psf_z2, round(p2.psfMagErr_u,3) as psfErr_u2,
round(p2.psfMagErr_g,3) as psfErr_g2, round(p2.psfMagErr_r,3) as psfErr_r2,
round(p2.psfMagErr_i,3) as psfErr_i2, round(p2.psfMagErr_z,3) as psfErr_z2,
p2.objid as objid2,

round(NN.distance*60,3) as theta

into mydb.binaryClose

from Neighbors as NN join star as p1 on p1.objid = NN.objid
join star as p2 on p2.objid = NN.neighborobjid
where NN.mode = 1 and NN.neighbormode = 1
and NN.type = 6 and NN.neighbortype = 6

and p1.psfMag_r between 14 and 20.5
and (p1.flags_g & '229802225959076') = 0 and (p1.flags_r & '229802225959076') = 0
and (p1.flags_i & '229802225959076') = 0 and (p1.flags_g & '268435456') > 0
and (p1.flags_r & '268435456') > 0 and (p1.flags_i & '268435456') > 0

and p2.psfMag_r between 14 and 20.5
and (p2.flags_g & '229802225959076') = 0 and (p2.flags_r & '229802225959076') = 0
and (p2.flags_i & '229802225959076') = 0 and (p2.flags_g & '268435456') > 0
and (p2.flags_r & '268435456') > 0 and (p2.flags_i & '268435456') > 0

and (p1.psfMag_r-p1.extinction_r) < (p2.psfMag_r-p2.extinction_r)
and (p1.psfMag_g-p1.extinction_g - p1.psfMag_i+p1.extinction_i)<
(p2.psfMag_g-p2.extinction_g - p2.psfMag_i+p2.extinction_i)

and NN.distance*60 between 3 and 4

select -- kinematic selection of candidate binaries

round(p1.ra,6) as ra1, round(p1.dec,6) as dec1, round(p1.extinction_r,3) as ext1,
round(p1.psfMag_u,3) as u1, round(p1.psfMag_g,3) as g1,
round(p1.psfMag_r,3) as r1, round(p1.psfMag_i,3) as i1,
round(p1.psfMag_z,3) as z1, round(p1.psfMagErr_u,3) as uErr1,
round(p1.psfMagErr_g,3) as gErr1, round(p1.psfMagErr_r,3) as rErr1,
round(p1.psfMagErr_i,3) as iErr1, round(p1.psfMagErr_z,3) as zErr1,
(case when ((p1.flags & '16') = 0) then 1 else 0 end) as ISOLATED1,
NN.objid as objid1,

round(p2.ra,6) as ra2, round(p2.dec,6) as dec2, round(p2.extinction_r,3) as ext2,
round(p2.psfMag_u,3) as u2, round(p2.psfMag_g,3) as g2,
round(p2.psfMag_r,3) as r2, round(p2.psfMag_i,3) as i2,
round(p2.psfMag_z,3) as z2, round(p2.psfMagErr_u,3) as uErr2,

```

```

round(p2.psfMagErr_g,3) as gErr2, round(p2.psfMagErr_r,3) as rErr2,
round(p2.psfMagErr_i,3) as iErr2, round(p2.psfMagErr_z,3) as zErr2,
(case when ((p2.flags & '16') = 0) then 1 else 0 end) as ISOLATED2,
NN.neighborobjid as objid2,

round(NN.distance*60,3) as theta,
round(s1.pmL,3) as pmL1, round(s1.pmB,3) as pmB1,
round(s2.pmL,3) as pmL2, round(s2.pmB,3) as pmB2

into mydb.binaryPM

from Neighbors as NN join star as p1 on p1.objid = NN.objid
join star as p2 on p2.objid = NN.neighborobjid
join propermotions as s1 on s1.objid = NN.objid
join propermotions as s2 on s2.objid = NN.neighborobjid

where NN.mode = 1 and NN.neighbormode = 1
and NN.type = 6 and NN.neighbortype = 6

and p1.psfMag_r between 14 and 19.5
and (p1.flags_g & '229802225959076') = 0 and (p1.flags_r & '229802225959076') = 0
and (p1.flags_i & '229802225959076') = 0 and (p1.flags_g & '268435456') > 0
and (p1.flags_r & '268435456') > 0 and (p1.flags_i & '268435456') > 0

and p2.psfMag_r between 14 and 19.5
and (p2.flags_g & '229802225959076') = 0 and (p2.flags_r & '229802225959076') = 0
and (p2.flags_i & '229802225959076') = 0 and (p2.flags_g & '268435456') > 0
and (p2.flags_r & '268435456') > 0 and (p2.flags_i & '268435456') > 0

and (p1.psfMag_r-p1.extinction_r) < (p2.psfMag_r-p2.extinction_r)
and (p1.psfMag_g-p1.extinction_g - p1.psfMag_i+p1.extinction_i)<
(p2.psfMag_g-p2.extinction_g - p2.psfMag_i+p2.extinction_i)

and s1.match = 1 and s2.match = 1
and s1.sigra < 350 and s1.sigdec < 350
and s2.sigra < 350 and s2.sigdec < 350
and sqrt(power(s1.pmL - s2.pmL,2) + power(s1.pmB - s2.pmB,2)) < 5
and (case when sqrt(power(s1.pmL,2) + power(s1.pmB,2)) >
sqrt(power(s2.pmL,2) + power(s2.pmB,2)) then
sqrt(power(s1.pmL,2) + power(s1.pmB,2)) else
sqrt(power(s2.pmL,2) + power(s2.pmB,2)) end) between 15 and 400

```

B. THE LIMITATIONS OF THE REDUCED PROPER MOTION DIAGRAM

Recent analysis of metallicity and kinematics for halo and disk stars by I08a provides sufficient information to understand the behavior of the reduced proper motion diagram in quantitative detail (including both the sequence separation and their widths), and to demonstrate that its efficiency for separating halo and disk stars deteriorates at distances beyond a few kpc from the Galactic plane. As Equation 8 shows, for a population of stars with the same v_t , the reduced proper motion is a measure of their absolute magnitude. For two stars with the same color that is sensitive to the effective temperature (such as the $g-i$ color), but with different metallicities and tangential velocities, the difference in their reduced proper motions is

$$\Delta r_{RPM} = r_{RPM}^H - r_{RPM}^D = \Delta M_r + 5 \log \left(\frac{v_t^H}{v_t^D} \right), \quad (\text{B1})$$

where H and D denote the two stars. In the limit that the *shape* of the photometric parallax relation does not depend on metallicity, ΔM_r does not depend on color, and is fully determined by the metallicity difference of the two stars (or populations of stars). Using metallicity distributions for disk and halo stars obtained by I08a, and their expression for $\Delta M_r([Fe/H])$ (Equation A2), we find that the expected offset between M_r for halo and disk stars with the same $g-i$ color varies from 0.6 mag for stars at 1 kpc from the Galactic plane to 0.7 mag at 5 kpc from the plane, where the variation is due to the vertical metallicity gradient for disk stars. The finite width of halo and disk metallicity distributions induces a spread of M_r (root-mean-square scatter computed using interquartile range) of 0.15 mag for disk stars and 0.18 mag for halo stars.

The effect of metallicity on the separation of halo and disk sequences in the reduced proper motion diagram is smaller than the effect of different tangential velocity distributions. Assuming for simplicity that stars are observed towards

a Galactic pole, and that the median heliocentric tangential velocities are 30 km s^{-1} for disk stars and 200 km s^{-1} for halo stars, the induced separation of their reduced proper motion sequences is $\sim 4.1 \text{ mag}$ (the expected scatter in the reduced proper motion due to finite velocity dispersion is $\sim 1\text{-}1.5 \text{ mag}$). Together with the $\sim 0.7 \text{ mag}$ offset due to different metallicity distributions, the separation of $\sim 5 \text{ mag}$ between the two sequences makes the reduced proper motion diagram a promising tool for separating disk and halo stars.

However, the reduced proper motion diagram is an efficient tool only for stars within 1-2 kpc from the Galactic plane. The main reason for this limitation is the decrease of rotational velocity for disk stars with distance from the Galactic plane, with a gradient of about $-30 \text{ km s}^{-1} \text{ kpc}^{-1}$ (see Section 3.4.2 in I08a). As the difference in rotational velocity between halo and disk stars diminishes with the distance from the plane, the separation of their reduced proper motion sequences decreases, too. A mild increase in the velocity dispersion of disk stars, as well as a decrease of their median metallicity with the distance from the plane, also decrease the sequence separation, but the dominant cause is the rotational velocity gradient.

To illustrate this effect, we select a sample of $\sim 60,000$ stars with $14 < r < 20$ and $0.2 < g - r < 0.4$, that are observed towards the north Galactic pole ($b > 70^\circ$). In this color range it is possible to separate disk and halo stars using photometric metallicity estimator from I08a, and we further select a sample of $\sim 16,000$ likely disk stars with $[Fe/H] > -0.9$, and a sample of $\sim 34,400$ likely halo stars with $[Fe/H] < -1.1$ (see Figure 9 in I08a for justification). Their proper motion distributions as functions of distance from the Galactic plane, Z , are shown in the top left panel in Figure 24. Because of the gradient in the rotational velocity for disk stars, their median proper motion becomes constant at $\sim 8 \text{ mas yr}^{-1}$ beyond $Z \sim 2 \text{ kpc}$, while the median proper motion for halo stars is roughly proportional to $1/Z$, with a value of $\sim 11 \text{ mas yr}^{-1}$ at $Z = 5 \text{ kpc}$.

The top right panel in Figure 24 shows the positions and widths of the reduced proper motion sequences for disk and halo stars as functions of Z , and the two bottom panels show the sequence cross-sections for stars with $Z = 1 - 1.5 \text{ kpc}$ and $Z = 3.5 - 4 \text{ kpc}$. At distances beyond $\sim 2 \text{ kpc}$ from the plane, the reduced proper motion diagram ceases to be an efficient tool for separating halo and disk stars because the two sequences start to significantly overlap. This increasing overlap is a result of the rotational velocity gradient for disk stars, and the finite width of halo and disk velocity distributions, and would be present even for *infinitely accurate* measurements (with the proper motion errors of $\sim 3 \text{ mas yr}^{-1}$ per coordinate, Munn et al. 2004, the sequence widths of $\sim 1.0\text{-}1.5 \text{ mag}$ are dominated by velocity dispersions). Hence, beyond $\sim 2 \text{ kpc}$ from the plane, metallicity measurements are necessary to reliably separate disk and halo populations.

The above analysis is strictly valid only for fields towards the north Galactic pole. Salim & Gould (2003) found that the position of disk and halo reduced proper motion sequences, relative to their positions at the north Galactic pole, varies with galactic latitude as

$$\Delta r_{RPM}(b) = 5 \log(v_t/v_t^{NGP}) = -1.43 (1 - \sin(|b|)), \quad (\text{B2})$$

where v_t^{NGP} is the median value of v_t for stars observed towards the north Galactic pole. This result is a bit unexpected because it does not contain longitudinal variation due to projection effects of the rotational motion of the local standard of rest. We show the variation of Δr_{RPM} , for stars with $0.2 < g - r < 0.4$, as a function of galactic coordinates in Figure 25. We use photometric metallicity to separate stars into disk and halo populations. As figure demonstrates, the longitudinal dependence is present for halo sample, but not for disk samples. We have generated simulated behavior of Δr_{RPM} using kinematic model from I08a, and reproduced the observed behavior to within the measurement noise. It turns out that the vertical gradient of rotational velocity for disk stars is fully responsible for the observed strong dependence of Δr_{RPM} on latitude, and which masks the dependence on longitude. Hence, the $\sin(|b|)$ term proposed by Salim & Gould (2003) is an indirect discovery of the vertical gradient of rotational velocity for disk stars! These empirical models also show that a linear dependence of $\Delta r_{RPM}(b)$ on $\sin(|b|)$ is only approximately correct, and that it ignores the dependence on distance. While a more involved best-fit expression is possible (full two-dimensional consideration of proper motion also helps to better separate disk and halo stars), we find that halo stars can always be efficiently rejected at $|b| > 30^\circ$, if the separator shown in Figure 5 is shifted upwards by 1 mag.

C. THE MODELING OF UNRESOLVED BINARIES IN THE SAMPLES OF WIDE BINARIES

One major uncertainty when using a photometric parallax relation is the lack of information whether the observed “star” is a single star, or a binary (multiple) system. If the observed “star” is a binary system, its luminosity will be underestimated, with the magnitude of the offset depending on the actual composition of the binary. To model this offset, or to correct for it, one would ideally like to have a probability density map that gives the probability of a magnitude offset, ΔM_r , as a function of the *observed* binary system’s color.

To construct such a map, we have generated a sample of 100,000 unresolved binary systems by randomly pairing stars drawn from the Kroupa, Tout & Gilmore (1990) luminosity function. By independently drawing the luminosities of each component to generate unresolved binary systems, we implicitly assume that the formation of each component is unaffected by the presence of the other. While there are other proposed mechanisms for binary formation (Clarke 2007, and references therein), we have chosen this one because it was easy to implement.

For every unresolved binary system we calculate the total r band luminosity, and the $r - i$ and $g - i$ color of the system. The magnitude offset, ΔM_r , caused by unresolved binarity, is obtained as the difference between the true r band absolute magnitude, and the absolute magnitude for the pair’s joint $r - i$ color calculated using Equation 15. The probability density map is then simply the number of unresolved binary systems (normalized with the total number

of systems at a given color) as a function of ΔM_r and pair's joint $g - i$ color, shown in Figure 26.

It is worth noting that, with the adopted binary formation mechanism, the magnitude offset is the smallest ($\Delta M_r < 0.1$ mag) for the bluest stars, and greatest ($\Delta M_r > 0.7$ mag) for the reddest stars. Because of this, the scatter due to unresolved binarity in the δ distribution should be more pronounced in a sample of red stars ($g - i > 2.0$), than in a sample of blue stars.

The map shown in Figure 26 can be parametrized as a Gaussian distribution $P(\Delta M_r|\mu, \sigma)$, where

$$\mu = 0.037 + 0.10(g - i) + 0.09(g - i)^2 - 0.012(g - i)^3 \quad (C1)$$

is the median ΔM_r , and

$$\sigma = 0.041 + 0.03(g - i) + 0.15(g - i)^2 - 0.057(g - i)^3 \quad (C2)$$

is the scatter (determined from the interquartile range). To verify the validity of this parametrization, we subtract ΔM_r and μ , normalize the difference with σ , find the distribution of such values, and fit a Gaussian to it. As shown in Figure 27, the distribution of normalized residuals is well described by a Gaussian with $\sigma = 0.9$. The two peaks in the distribution are due to highly asymmetric distributions of ΔM_r values around the median ΔM_r for the bluest ($g - i \sim 0.1$) and reddest ($g - i \sim 2.9$) systems.

To create a sample of wide binaries where some of the stars are unresolved binary systems, first we select pairs with $20'' < \theta < 30''$ from the initial sample of stellar pairs. Following the procedure described in Section 3.2, we create the “true” wide binaries by changing the r_2 magnitude using Equation 11, and add 0.15 mag of Gaussian noise to simulate the scatter in the photometric parallax due to photometric errors. A fraction of stars is then randomly converted to unresolved binary systems by subtracting a ΔM_r value from the r band (apparent) magnitude, where the ΔM_r is drawn from a $g - i$ color-dependent $P(\Delta M_r|\mu, \sigma)$ distribution.

Figure 28 shows the δ distribution for such a mock sample, where the components are redder than $g - i = 2.0$ and have a 40% probability to be unresolved binary systems. Different configurations of single stars and unresolved binaries that contribute to the observed δ distribution can be easily identified. Wide binaries where both components are single stars contribute the central narrow Gaussian, with its width due to photometric errors. If the brighter component is an unresolved binary system, its absolute magnitude is underestimated, and the result is an offset in δ in the negative direction. A similar outcome happens if the fainter component is an unresolved binary system, but the offset is positive. Single star-unresolved binary configurations, therefore, contribute the left and the right Gaussians. If both components are unresolved binary systems, the δ will be centered on zero and will be $\sigma_0\sqrt{2}$ wide, where σ_0 is the width of the $(\Delta M_r - \mu)$ distribution. This behavior is consistent with the δ distributions observed in Figure 12.

REFERENCES

- Adelman-McCarthy, J. K. et al. 2008, *ApJS*, 175, 297
 Allen, C., Poveda, A., & Herrera, M. 2000, *A&A*, 356, 529
 Allen, C., Poveda, A., & Hernández-Alcántara, A. 2007, in *IAU Symp. 240, Binary Stars as Critical Tools & Test in Contemporary Astrophysics*, ed. B. Hartkopf, E. Guinan, & P. Harmanec, 405
 Andersen, J. 1991, *ARA&A*, 3, 91
 Bahcall, J. N. & Soneira, R. M. 1981, *AJ*, 246, 122
 Bochanski, J. et al. 2008, in prep
 Chanamé, J. 2007, in *IAU Symp. 240, Binary Stars as Critical Tools & Tests in Contemporary Astrophysics*, ed. B. Hartkopf, E. Guinan, & P. Harmanec, 1
 Chanamé, J. & Gould, A. 2004, *ApJ*, 601, 289
 Clarke, C. J. 2007, in *IAU Symp. 240, Binary Stars as Critical Tools & Tests in Contemporary Astrophysics*, ed. B. Hartkopf, E. Guinan, & P. Harmanec, 337
 Covey, K. R., et al. 2007, *AJ*, 134, 2398
 Couteau, P. 1960, *J. des Observateurs*, 43, 41
 Croll, B. 2006., *PASP*, 118, 1351
 Duquenois, A. & Mayor, M. 1991, *A&A*, 248, 485
 Finlator, K. et al. 2000, *AJ*, 120, 2615
 Fischer, D. A. & Marcy, G. W. 1992, *ApJ*, 396, 178
 Flaugher, B. & the Dark Energy Survey Collaboration 2007, *BAAS*, 209, 22.01
 Ford, E. B. 2005, *AJ*, 129, 1706
 Gelman, A. & Rubin, D. 1992, *Stat. Sci.*, 7, 457
 Giersz, M. 2006, *MNRAS*, 371, 484
 Gould, A. 1995, *ApJ*, 440, 510
 Gould, A., & Salim, S. 2003, *ApJ*, 582, 1001
 Gunn, J. E. et al. 1998, *AJ*, 116, 3040
 Gunn, J. E. et al. 2006, *AJ*, 131, 2332
 Hastings, W. K. 1970, *Biometrika*, 57, 97
 Hawley, S. L. et al. 2002, *AJ*, 123, 3409
 Heggie, D. C. 1975, *MNRAS*, 173, 729
 Helmi, A. et al. 2003, *ApJ*, 586, 195
 Hogg, D. W., Finkbeiner, D. P., Schlegel, D. J. & Gunn, J.E. 2002, *AJ*, 122, 2129
 Hurley, J. R., Aarseth, S. J., & Shara, M. M. 2007, *ApJ*, 665, 707
 Ivezić, Ž. et al. 2003, *Mem. Soc. Astron. Italiana*, 74, 978
 Ivezić, Ž. et al. 2004, *Astron. Nachr.*, 325, 583
 Ivezić, Ž., Vivas, A. K., Lupton, R. H., & Zinn, R. 2005, *AJ*, 129, 1096
 Ivezić, Ž. et al. 2008a, accepted to *ApJ*(also astro-ph/0804.3850)
 Ivezić, Ž. et al. 2008b, astro-ph/0805.2366
 Jurić, M. et al. 2008, *ApJ*, 673, 864
 Kaiser, N. et al. 2002, *Proc. SPIE*, 4836, 154
 Keller, S.C. et al. 2007, 24, 1
 Kroupa, P., Tout, C. A. & Gilmore, G. 1990, *MNRAS*, 244, 76
 Laird, J. B., Carney, B. W & Latham, D. W. 1988, *AJ*, 95, 1843
 Lenz, D. D., Newberg, J., Rosner, R., Richards, G. T., & Stoughton, C. 1998, *ApJS*, 119, 121
 Lépine, S. & Bongiorno, B. 2007, *AJ*, 133, 889
 Lupton, R. H., Ivezić, Ž., Gunn, J. E., Knapp, G. R., Strauss, M. A. & Yasuda, N. 2002 *Proc. SPIE*, 4836, 350
 Luyten, W. J. 1979, *New Luyten Catalog of Stars with Proper Motions Larger than Two Tenths of an Arcsecond* (Minneapolis: Univ. of Minnesota Press)
 Minkowski, A. & Abell, G. O. 1963, in *Stars and Stellar Systems*, Vol. 3
 Metropolis, N., Rosenbluth, A. W., Rosenbluth, M. N., Teller, A. H., & Teller, E., *J. Chem. Phys.*, 21, 1087
 Monet, D. G. et al. 2003, *AJ*, 125, 984
 Munn, J. A. et al. 2004, *AJ*, 127, 3034
 Öpik, E. J. 1924, *Tartu Obs. Publ.* 25, No. 6
 Perryman, M. A. C. et al. 2001, *A&A*, 369, 339
 Pier, J. R., Munn, J. A., Hindsley, R. B., Hennesy, G. S., Kent, S. M., Lupton, R. H. & Ivezić, Ž. 2003, *AJ*, 125, 1559
 Poveda, A. et al. 1994, *Revista Mexicana de Astronomía y Astrofísica*, 28, 43

- Poveda, A., Allen, C. & Hernández-Alcántara, A. 2007, in IAU Symp. 240, Binary Stars as Critical Tools & Test in Contemporary Astrophysics, ed. B. Hartkopf, E. Guinan, & P. Harmanec, 417
- Press, W. H., Teukolsky, S. A., Vetterling, W. T., & Flannery, B. P. 1992, *Numerical Recipes in C* (2nd ed.; New York: Cambridge Univ. Press)
- Reid, I. N. et al. 1991, *PASP*, 103, 661
- Ribas, I. 2006, *ASP Conf.* 349, 55
- Richards, G. T. et al. 2002, *AJ*, 123, 2945
- Salim, S. & Gould, A. 2003, *ApJ*, 582, 1011
- Schlegel, D., Finkbeiner, D. P., & Davis, M. 1998, *ApJ*500, 525
- Scranton, R. et al. 2002, *ApJ*, 579, 48
- Sesar, B. et al. 2007, *AJ*, 134, 2236
- Siegel, M. H., Majewski, S. R., Reid, I. N. & Thompson, I. B. 2002, *ApJ*, 578, 151
- Sirko, E. et al. 2004, *AJ*, 127, 899
- Smith, J. A. et al. 2002, *AJ*, 123, 2121
- Stoughton, C. et al. 2002, *AJ*, 123, 485
- Tegmark, M. et al. 2004, *Phys. Rev. D*, 69, 103501
- Tucker, D. et al. 2006, *Astron. Nachr.*, 327, 821
- Weinberg, M. D, Shapiro, S. L., & Wasserman, I. 1987, *ApJ*, 312, 367
- West, A. A., Walkowicz, L. M. & Hawley, S. L. 2005, *PASP*, 117, 706
- Wilkinson, M. I. et al. 2005, *MNRAS*, 359, 1306
- Yanny, B. et al. 2000, *ApJ*, 540, 825
- Yoo, J., Chanamé, J. & Gould, A. 2004, *ApJ*, 601, 311

TABLE 1
 THE CENTERS, WIDTHS, AND AREAS FOR BEST-FIT GAUSSIAN DISTRIBUTIONS

	Geometrically-selected sample		Kinematically-selected sample	
	Narrow Gaussian	Wide Gaussian	Narrow Gaussian	Wide Gaussian
Center	-0.01	-0.03	-0.05	0.01
Width	0.12	0.54	0.11	0.51
Area ^a	0.26	0.74	0.34	0.66

^a Areas of the narrow and wide Gaussians sum to 1

TABLE 2
 THE CONDITIONAL PROBABILITY DENSITY
 FUNCTIONS
 $P[(g-i)_B|(g-i)_A] = a + b(g-i) + c(g-i)^2$

Best-fit parameters			
$(g-i)_A$ bin	a	b	c
$0.4 < (g-i)_A < 0.8$	0.38	0	0
$0.8 < (g-i)_A < 1.2$	0.46	0	0
$1.2 < (g-i)_A < 1.6$	0.37	0	0
$1.6 < (g-i)_A < 2.0$	0.37	0	0
$2.0 < (g-i)_A < 2.4$	0.08	0.14	0.04
$2.4 < (g-i)_A < 2.8$	0.23	-0.50	0.38

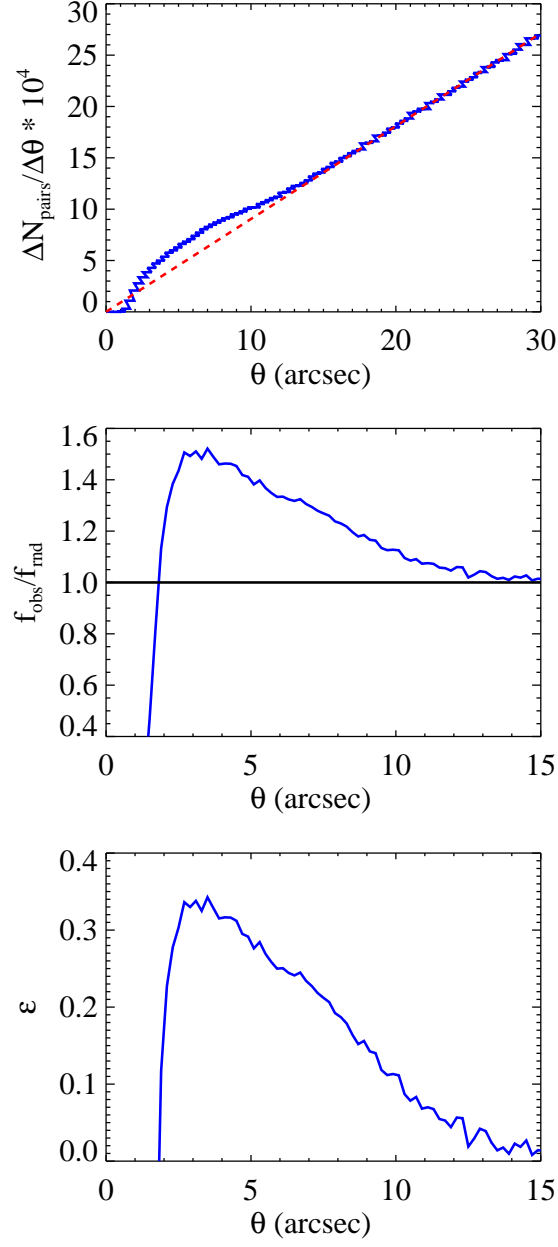


FIG. 1.— *Top*: A comparison of observed (f_{obs} , solid histogram) and random (f_{rnd} , dashed line, see text) distributions of angular separation θ . *Middle*: Ratio $f_{\text{obs}}/f_{\text{rnd}}$ as a function of angular separation θ . *Bottom*: Fraction of true binary systems, ϵ , as a function of angular separation θ .

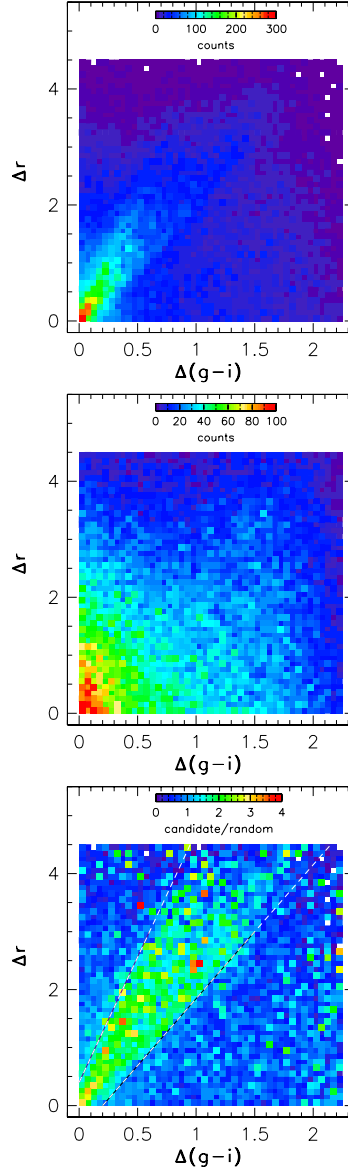


FIG. 2.— Distribution of counts for the geometrically-selected candidate sample (*top*), random sample (*middle*), and the ratio of two maps (*bottom*) in the $\Delta r = r_2 - r_1$ vs. $\Delta(g-i) = (g-i)_2 - (g-i)_1$ diagram, binned in 0.05×0.1 mag bins. The average candidate-to-random ratio in the region outlined by the dashed lines (Eq. 3 and 4) is ~ 1.7 , implying that $> 40\%$ of candidates are true binaries.

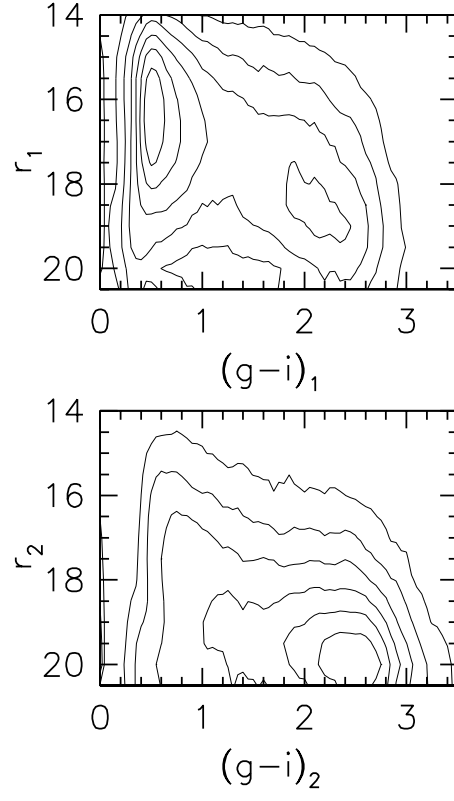


FIG. 3.— The r vs. $g-i$ distribution of brighter (*top*) and fainter (*bottom*) components from the geometrically-selected sample of candidate binaries, shown with linearly spaced contours.

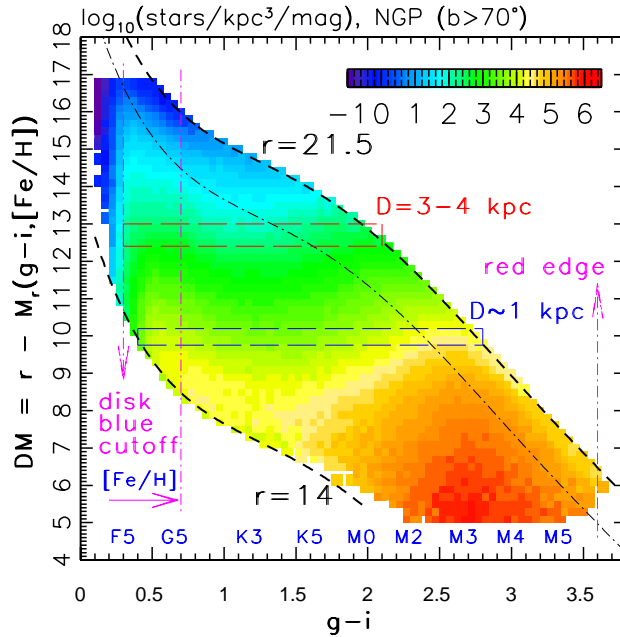


FIG. 4.— The color-coded map, with the legend shown in the top right corner, shows the logarithm of the volume number density (stars/kpc³/mag) of ~ 2.8 million stars with $14 < r < 21.5$ observed towards the north Galactic pole ($b > 70^\circ$), as a function of their distance modulus and the $g-i$ color (the density variation in the horizontal direction represents luminosity function, and the variation in the vertical direction reflects the spatial volume density profiles of disk and halo stars). The absolute magnitudes are computed using expressions A3 and A7 from I08a, and the displayed distance range is 100 pc to 25 kpc. Stars are color-selected from the main stellar locus (dominated by main-sequence stars) using criteria 3-5 from Section 2.3.1 in I08a. The metallicity correction is applied using photometric metallicity for stars with $g-i < 0.7$ (based on Eq. 4 from I08a), and by assuming $[Fe/H] = -0.6$ for redder stars. As illustrated above the $g-i$ axis using the MK spectral type vs. $g-i$ color table from Covey et al. (2007), this color roughly corresponds to G5. The two vertical arrows mark the turn-off color for disk stars, and the red edge of M dwarf color distribution (there are redder M dwarfs detected by SDSS, but their volume number density, i.e., the luminosity function, falls precipitously beyond this limit; J. Bochanski, priv. comm.). The two diagonal dashed lines show the apparent magnitude limits, $r = 14$ and $r = 21.5$. The dot-dashed diagonal line corresponds to $r = 20$, which approximately describes the 50% completeness limit for stars with cataloged proper motions (Munn et al. 2004). Around the marked distance range of 3-4 kpc, the counts of halo stars begin to dominate disk stars (see Fig. 6 in I08a), and the distance range around 1 kpc offers the largest color completeness.

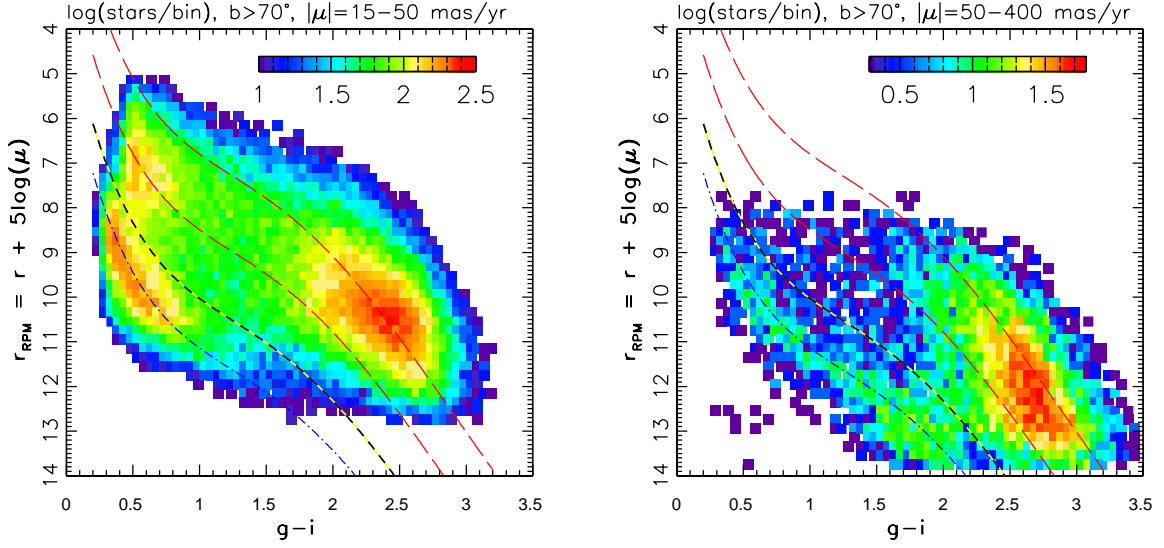


FIG. 5.— The reduced proper motion diagrams for two subsamples of stars shown in Fig. 4. The color-coded maps show the logarithm of the number of stars per pixel, according to the legends. The left panel corresponds to a sample of $\sim 446,000$ stars with proper motions in the range 15-50 mas/yr, and the right panel to a sample of 43,000 stars from the range 50-400 mas/yr. The requirement of larger proper motions introduces bias towards closer, and thus redder stars. Two long-dashed lines in each panel correspond to photometric parallax relation from I08a, evaluated for $[Fe/H] = -0.6$ and with tangential velocity of 55 km/s (top curve) and 120 km/s (bottom curve). This variation of tangential velocity is consistent with the rotational velocity gradient discussed by I08a. The dot-dashed line is evaluated for $[Fe/H] = -1.5$ and with tangential velocity of 300 km/s. The short-dashed line (second from the bottom) separates disk and halo stars, and is evaluated for $[Fe/H] = -1.5$ and with tangential velocity of 180 km/s.

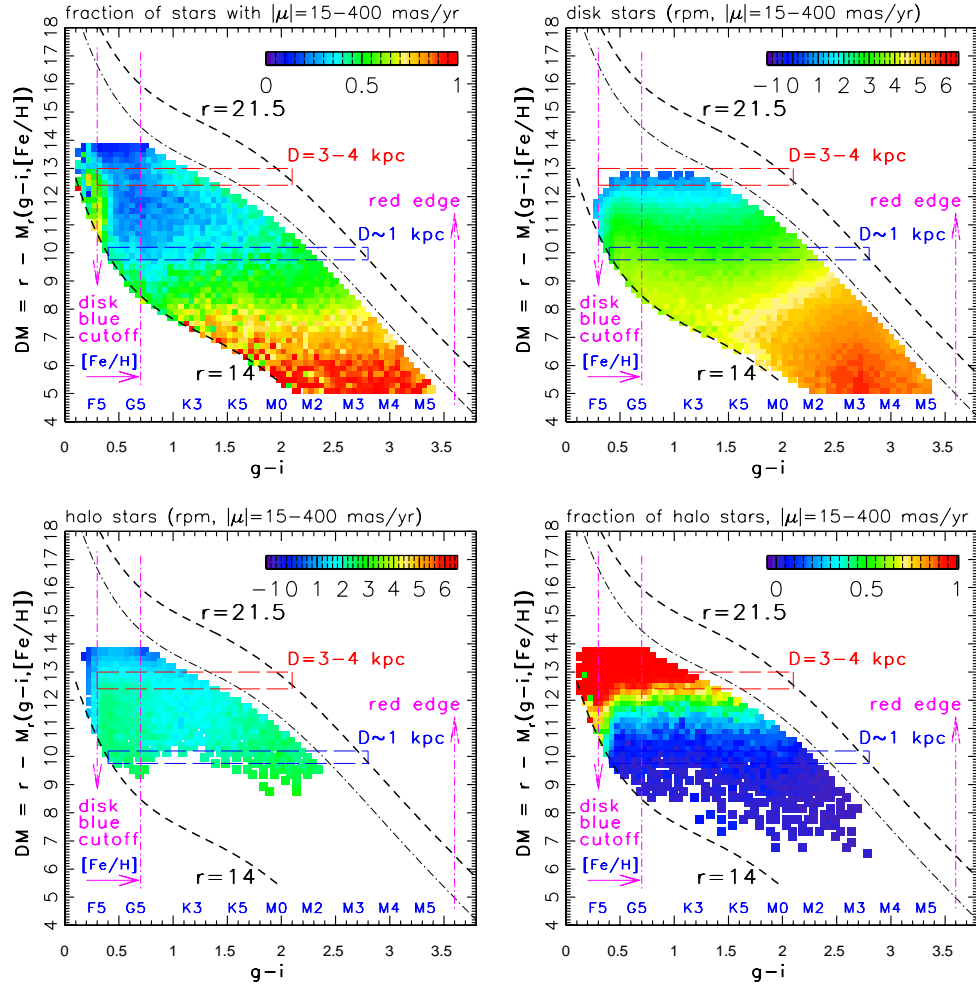


FIG. 6.— Analogous to Fig. 4, for subsamples selected using proper motion measurements. Out of 2.8 million stars shown in Fig. 4, 1.24 million are brighter than $r = 19.5$ and have proper motion measurements. Of those, 498,000 have proper motion in the range 15-400 mas/yr (only 10% of selected stars have proper motions greater than 50 mas/yr). The color-coded map in the top left panel shows the fraction of such stars, as a function of distance and the $g - i$ color. At a distance of ~ 1 kpc, about half of all stars have proper motion larger than 15 mas/yr. The top right panel shows the counts of candidate disk stars, selected as stars above the separator shown in Fig. 5, and the bottom left panel shows halo stars selected from below the separator. The bottom right panel shows the counts of halo stars, as a fraction of all stars selected using the reduced proper motion diagram. Note that beyond 3 kpc, the sample is dominated by halo stars.

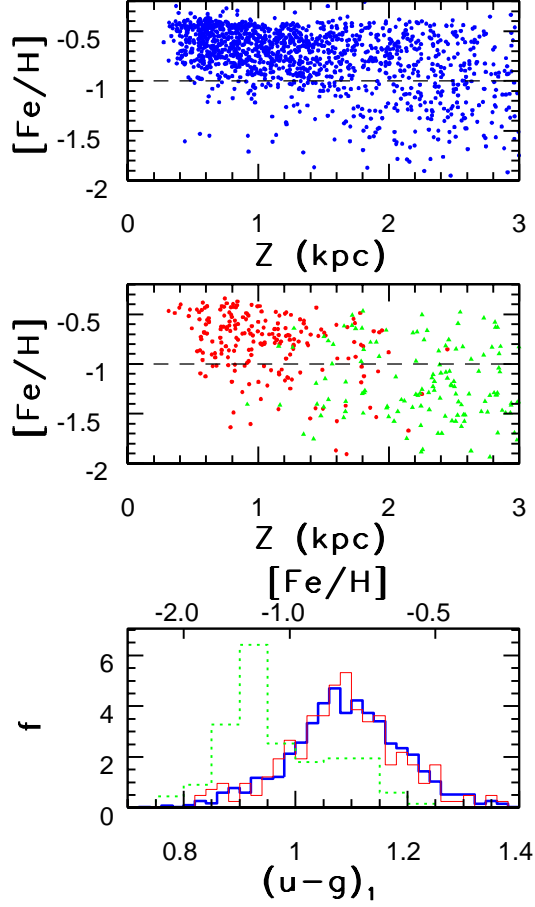


FIG. 7.— *Top*: The photometric metallicity vs. distance from the Galactic plane diagram for candidate binaries selected from the geometric sample using $|\delta| < 0.4$ and $0.2 < (g-r)_1 < 0.4$. The $|\delta| < 0.4$ cut is used to reduce the contamination by random pairs (see Section 3.6). Note that the fraction of low-metallicity halo binaries ($[Fe/H] < -1$) becomes significant only at $Z > 2$ kpc. *Middle*: Analogous to the top panel, except that binaries from the kinematic sample are shown. Dots correspond to binaries with reduced proper motions characteristic of disk binaries, and triangles to candidate halo binaries. Note that binaries with disk-like metallicity ($[Fe/H] > -1$) at large distances ($Z > 2$ kpc) are misclassified as halo binaries. *Bottom*: The comparison of the $(u-g)_1$ color distributions, and corresponding photometric metallicity distributions, for binaries from the top two panels. The metallicity vs. $u-g$ color transformation is taken from I08a. The distribution for binaries from the geometric sample is shown by the thick solid line, and the distributions for binaries from the kinematic sample are shown by the thin solid line (disk candidates) and dotted line (halo candidates).

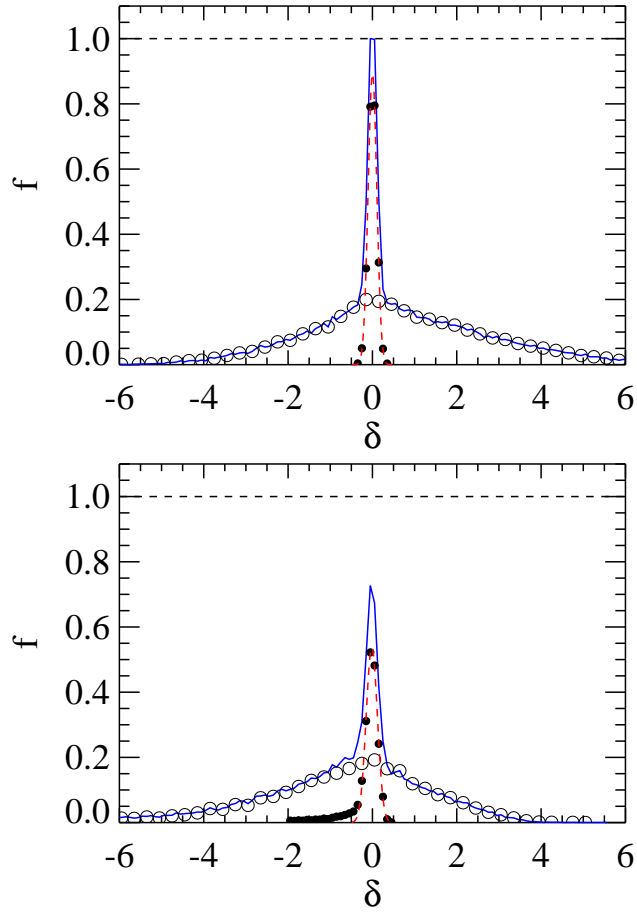


FIG. 8.— Distribution of $\delta = (M_{r,2} - M_{r,1}) - (r_2 - r_1)$ values for a mock sample of candidate binaries (*solid line*) when $M_r = M_r(r - i|\mathbf{p}_0)$ (*top*), and for a M_r different from $M_r(r - i|\mathbf{p}_0)$ (*bottom*). The fraction of random pairs (the contamination) in the sample is 80%. The δ distribution for “true” binaries (*dots*) is obtained by subtracting the δ distribution of random pairs (*open circles*) from the candidate binary δ distribution. The best-fit Gaussian for the “true” binaries δ distribution is centered on 0 and 0.1 mag wide in the top panel, and centered on -0.02 and 0.13 mag wide in the bottom panel.

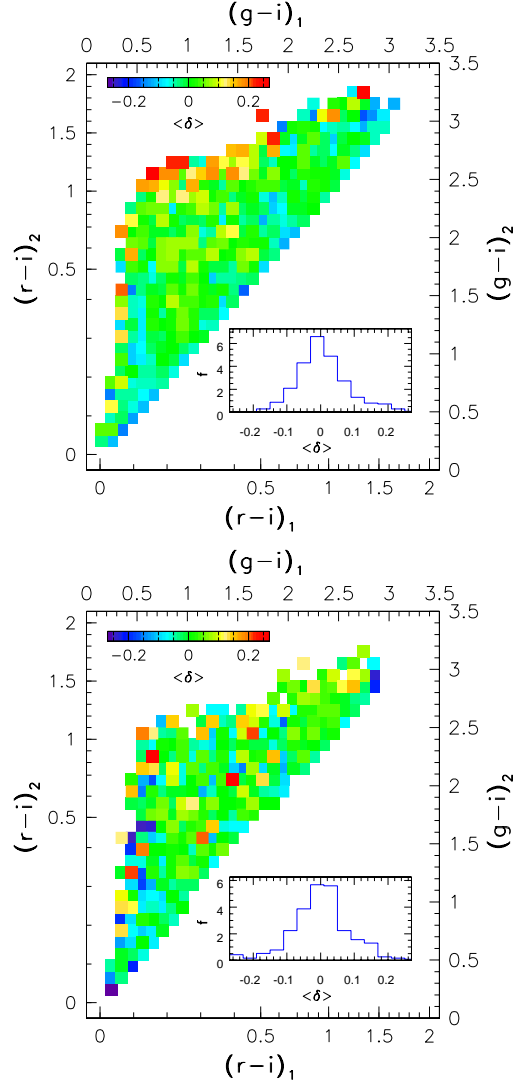


FIG. 9.— The dependence of median δ , $\langle \delta \rangle$, values on $r-i$ colors of the brighter and fainter component for the geometrically- (*top*) and kinematically-selected (*bottom*) samples of candidate binaries with $|\delta| < 0.4$. The $r-i$ color axes are interpolated from $g-i$ axes using Eq. 10. Sources are binned in 0.1×0.1 mag $g-i$ color pixels (minimum of 6 sources per pixel), and the median values are color-coded according to the legends given at the top of each panel. Inset histograms show the distribution of $\langle \delta \rangle$. The $\langle \delta \rangle$ distribution medians are 0 to within < 0.01 mag, and the scatter (determined from the interquartile range) is 0.07 mag for both samples.

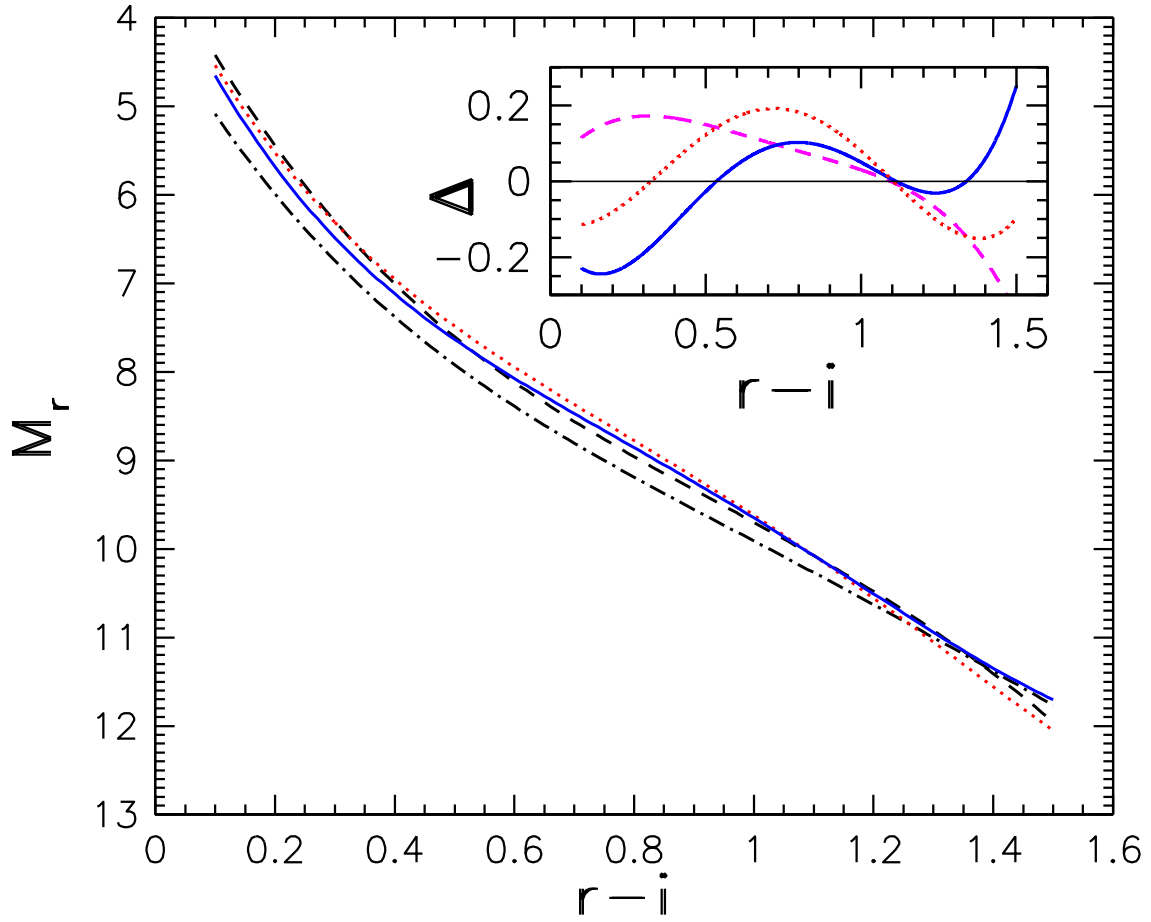


FIG. 10.— Comparison of Eq. 14 (*dot-dashed line*) and Eq. 15 (*dashed line*) photometric parallax relations from J08 (their Eqs. 1 and 2) with Eq. 12 (*solid line*) and Eq. 13 (*dotted line*) photometric parallax relations determined in this work. The inset shows the magnitude difference, $\Delta = M_{J08} - M_{S08}$, between the Eq. 15 photometric parallax relation, and Eqs. 12 (*solid line*) and 13 (*dotted line*) from this work. The rms scatter between Eqs. 12 and 13, and Eq. 15, is 0.13 mag. The rms scatter between Eqs. 12 and 13 (*dashed line*) is also 0.13 mag.

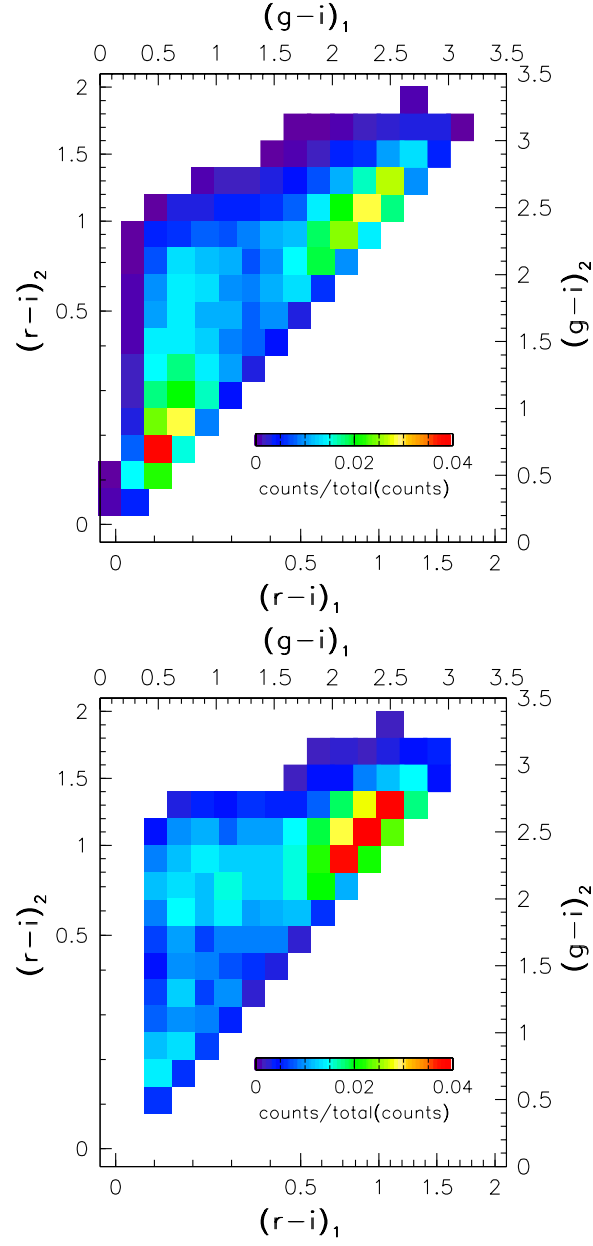


FIG. 11.— A comparison of $(g-i)_2$ vs. $(g-i)_1$ color-color distributions of geometrically-selected (*top*) and kinematically-selected disk binaries (*bottom*) with $|\delta| < 0.4$. The fraction of binaries in a pixel is color-coded according to legends. The pixels are 0.2×0.2 mag wide in $g-i$ color, and the $r-i$ color axes are interpolated from $g-i$ axes using Eq. 10.

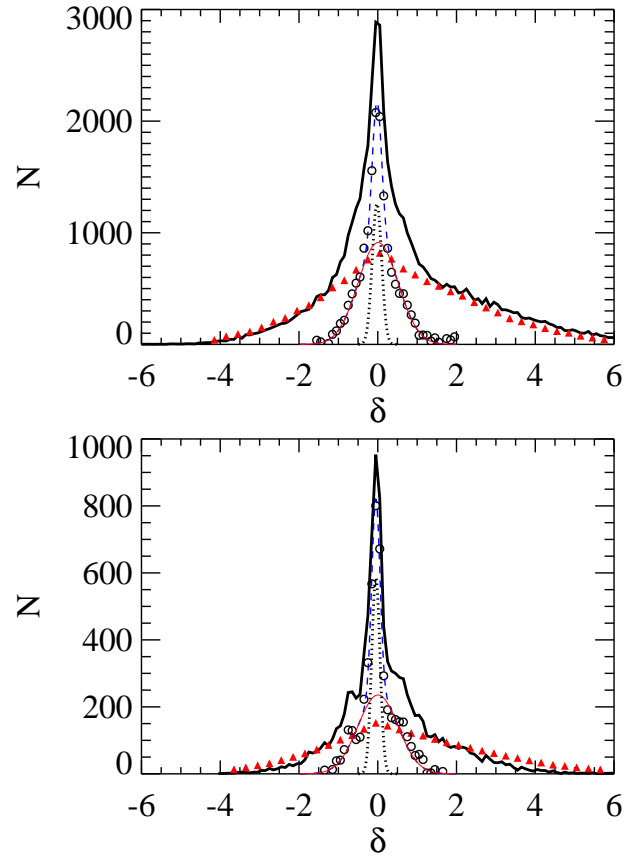


FIG. 12.— Distribution of δ values for the geometrically- (*top*) and kinematically-selected (*bottom*) samples of candidate binaries, with absolute magnitudes, M_r , calculated using Eqs. 12 and 13, respectively. The δ distribution for true binaries (*open circles*) is obtained by subtracting the δ distribution of random pairs (*triangles*) from the δ distribution for candidate binaries (*thick solid line*). The δ distribution for true binaries is a non-Gaussian distribution (*dashed line*), that can be described as a sum of two Gaussian distributions. The centers, widths, and areas for the best-fit narrow (*dotted line*) and wide (*thin solid line*) Gaussian distributions are given in Table 1. The integrals (areas) of δ distributions for random pairs and candidate binaries are A_{random} and $A_{observed}$, respectively.

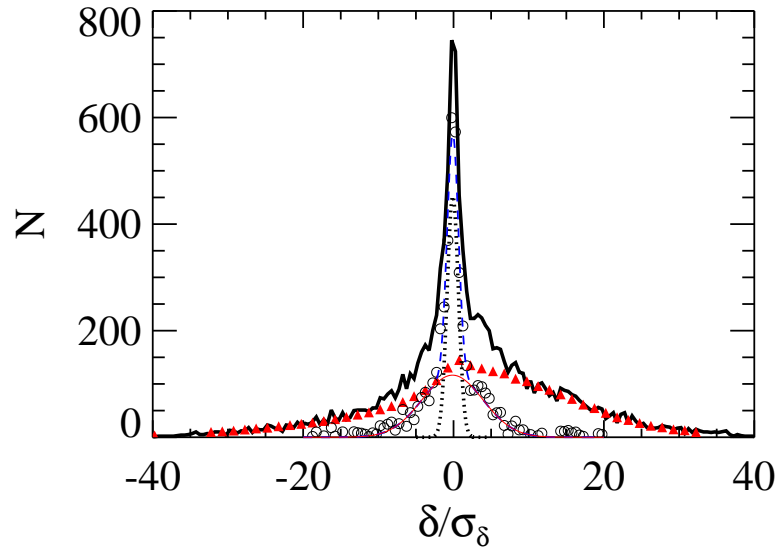


FIG. 13.— Distribution of δ values normalized by the expected formal errors, σ_δ , for the kinematically-selected sample of candidate binaries. The δ/σ_δ distribution for true binaries (*open circles*) is obtained by subtracting the δ/σ_δ distribution of random pairs (*triangles*) from the δ/σ_δ distribution for candidate binaries (*thick solid line*). The δ/σ_δ distribution for true binaries is a non-Gaussian distribution (*dashed line*), that can be described as a sum of two Gaussian distributions. The best-fit narrow Gaussian (*dotted line*) is 0.75 wide and centered on -0.10, while the best-fit wide Gaussian (*thin solid line*) is 4.04 wide and centered on -0.14.

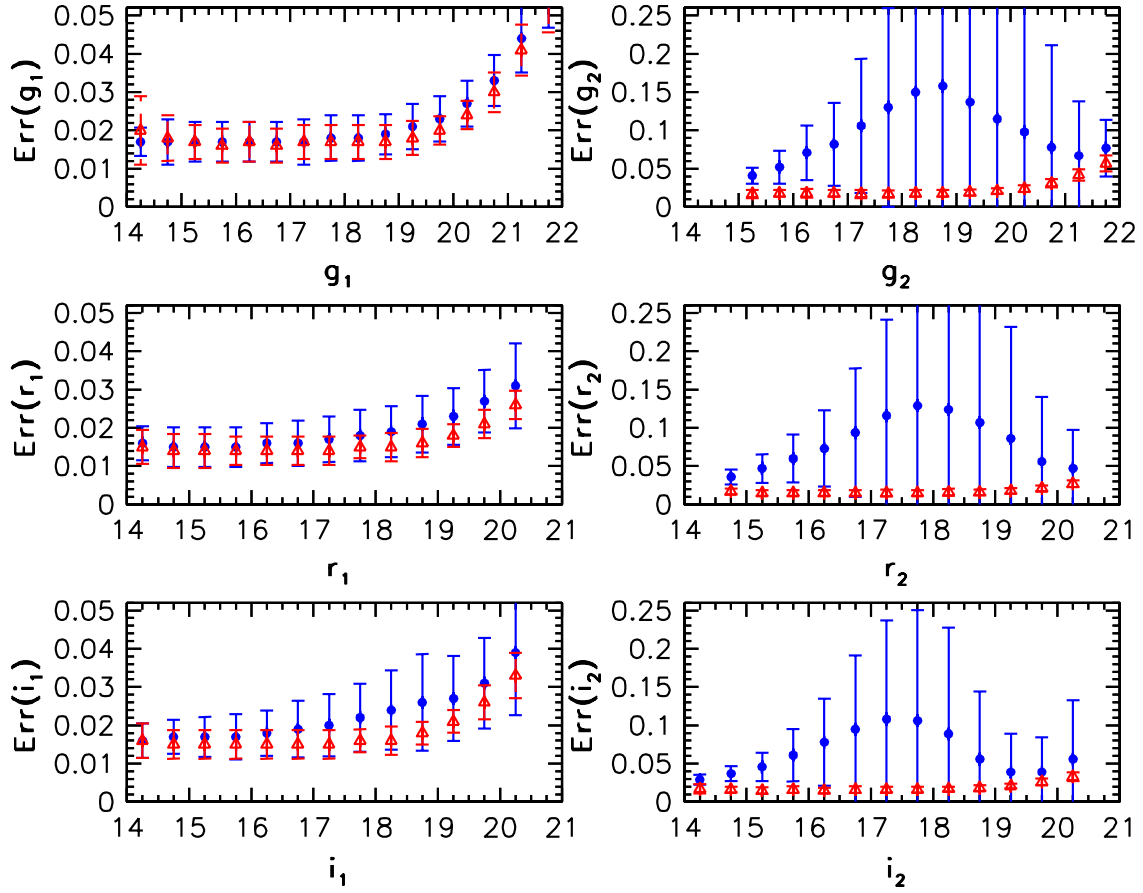


FIG. 14.— Dependence of median PSF magnitude errors on magnitude for the brighter (*left*) and fainter (*right*) components in the geometrically- (*dots*) and kinematically-selected (*triangles*) samples of candidate binaries. The vertical bars show the rms scatter in each bin (not the error of the median which is much smaller). The fainter components of geometrically-selected candidate binaries have overestimated median PSF magnitude errors when compared to the kinematically-selected binaries.

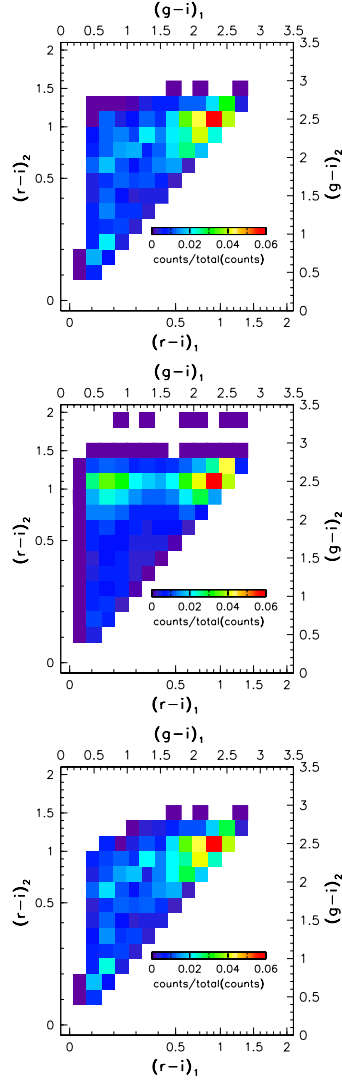


FIG. 15.— The fraction of $|\delta| < 0.4$ binaries in $0.7 < d/kpc < 1.0$ volume-complete geometrically-selected (*top*) and random (*middle*) samples that have $(g-i)_1$ and $(g-i)_2$ as the colors of the brighter and fainter component. The pixels are 0.2×0.2 mag wide in $g-i$ color, and the $r-i$ color axes are interpolated from $g-i$ axes using Eq. 10. The pixels in maps sum to 1. The bottom plot shows the difference, $f_{cand}[(g-i)_1, (g-i)_2] - C * f_{rand}[(g-i)_1, (g-i)_2]$, between the two maps, where $C = 0.14$ is the fraction of random pairs estimated using Eq. 21 for the $|\delta| < 0.4$, $0.7 < d/kpc < 1.0$ geometrically-selected sample. The pixels with negative values are not shown and the map is renormalized so that the pixels sum to 1.

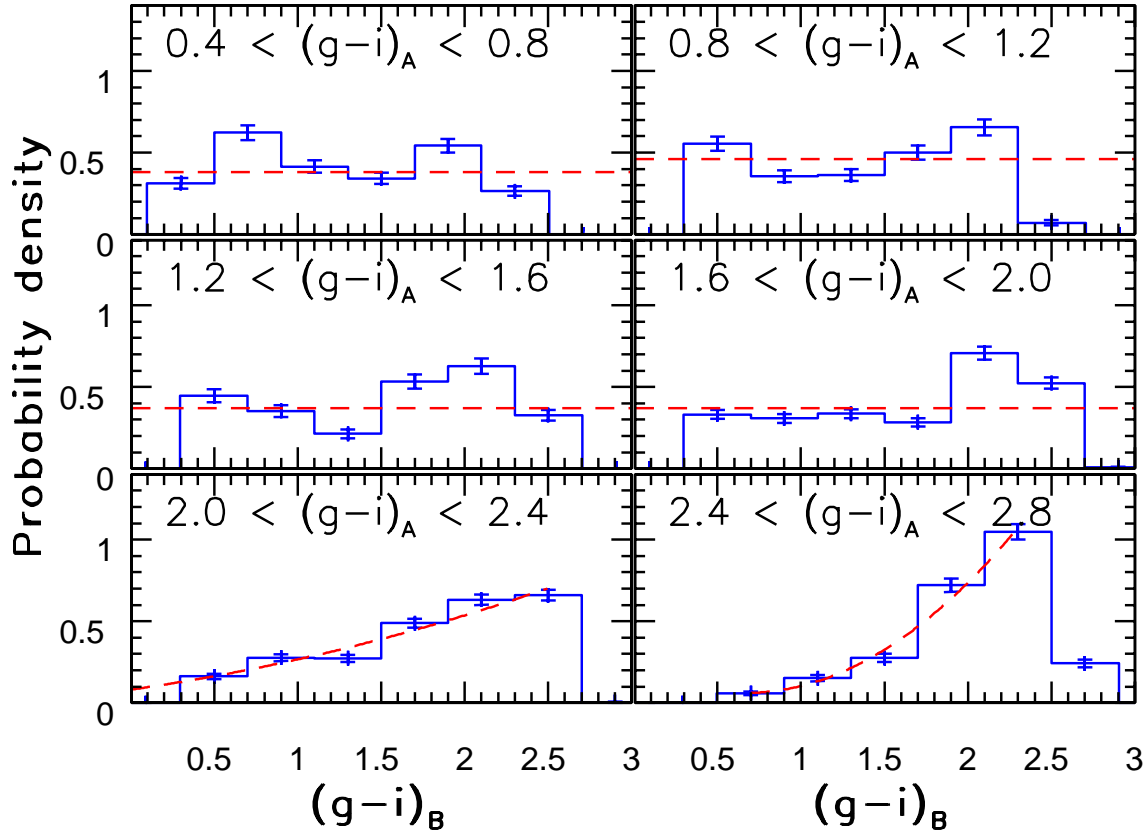


FIG. 16.— Conditional probability density of having one component with $(g-i)_B$ color in a wide binary system where the other component has $(g-i)_A$. The conditional probability density for $(g-i)_A < 2.0$ (*top* and *middle*) is independent of $(g-i)_B$, while for $(g-i)_A > 2.0$ (*bottom*) it changes as a square of $(g-i)_B$. The best-fit functions describing these conditional probabilities are given in Table 2.

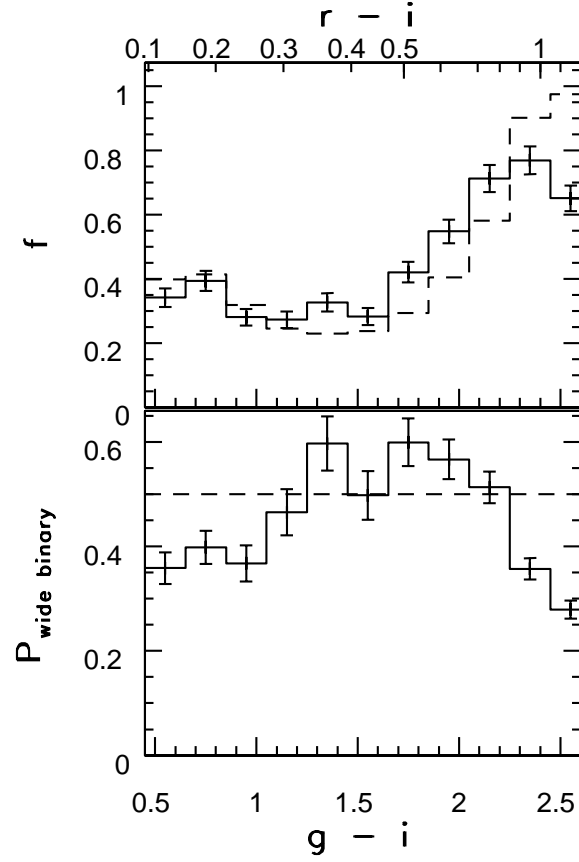


FIG. 17.— *Top:* A comparison of $g - i$ color distribution of stars in the $|\delta| < 0.4$, $0.7 < d/kpc < 1.0$ volume-complete, geometrically-selected, wide binary sample (*solid line*), and of all stars in the same volume (*dashed line*). The distributions are normalized to an area of 1, and the error bars show the Poisson noise. *Bottom:* The probability density for finding a star with $g - i$ color in a wide binary system, $P[(g - i)_A] = P_{\text{widebinary}}$, calculated as a ratio of the two distributions from the top panel, and renormalized to an area of 1. The equal probability distribution is shown as the dashed line.

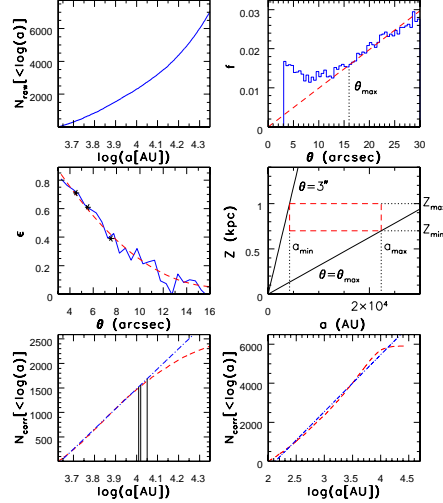


FIG. 18.— *Top left:* The cumulative distribution of $\log(a)$ for geometrically-selected candidate binaries with $|\delta| < 0.2$ and $0.7 < Z/\text{kpc} < 1.0$, where a is the average semi-major axis. *Top right:* The differential distribution of angular separation, θ , for geometrically-selected candidate binaries with $|\delta| < 0.2$ and $0.7 < Z/\text{kpc} < 1.0$. The distribution of random pairs (*dashed line*) is obtained by fitting a linear function $f_{\text{rnd}}(\theta) = C\theta$ to the observed histogram for $\theta > 18''$. θ_{max} is defined as the angular separation for which the fraction of true binaries falls below $\sim 5\%$. *Middle left:* The fraction of true binaries, ϵ (*solid line*), calculated from the θ distribution using Eq. 2 (see Section 2.3) for the $0.7 < Z/\text{kpc} < 1.0$ sample, is modeled as a second-degree polynomial, $\epsilon(\theta)$ (*dashed line*). For three θ -selected subsamples ($4'' - 5''$, $5'' - 6''$, and $7'' - 8''$), the fraction of true binaries was also calculated using Eq. 21 (i.e., from the δ distribution) and is shown with symbols. *Middle right:* The box (*dashed lines*) shows the allowed range in a defined by Z_{min} , Z_{max} , and θ_{max} (see Eqs. 23 and 24). Only binaries within this a range are considered when plotting the corrected cumulative distribution of $\log(a)$. *Bottom left:* The cumulative distribution of $\log(a)$ for candidate binaries with $|\delta| < 0.2$ and $0.7 < Z/\text{kpc} < 1.0$ (*dashed line*), corrected using $\epsilon(\theta)$ to account for the decreasing fraction of true binaries at large $\theta \propto a/d$ separations. The vertical lines show $\log(a)$ for which the straight line fit (*dot-dashed line*) to the cumulative distribution deviates by more than 1.0% ($\log(a_{\text{low}})$), 1.5% ($\log(a_{\text{break}})$), and 2.0% ($\log(a_{\text{high}})$). *Bottom right:* The corrected cumulative distribution of $\log(a)$ for mock candidate binaries created using the $f(a) \propto a^{-0.8}$ distribution limited to $a_1 = 100$ AU and $a_2 = 10000$ AU.

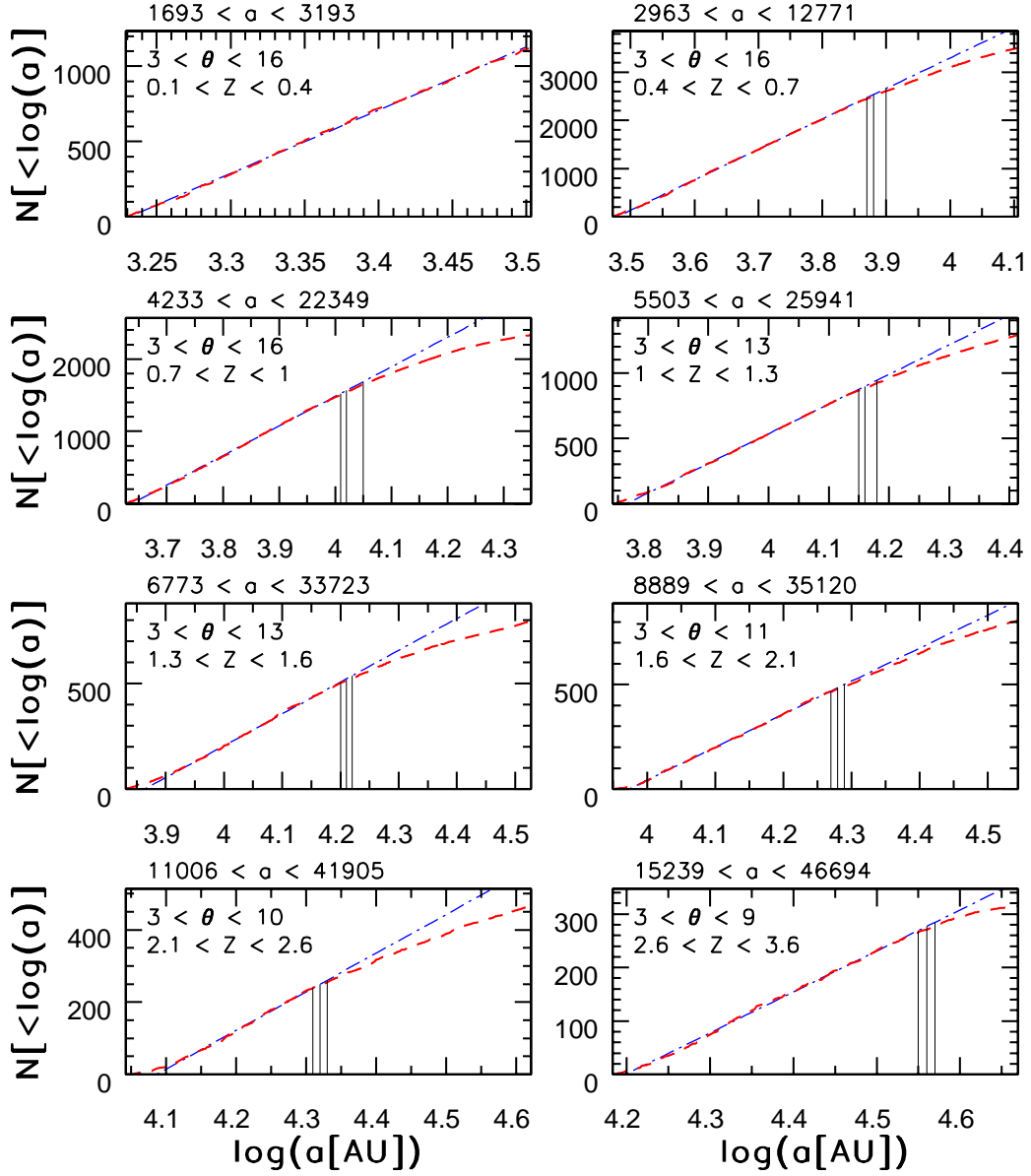


FIG. 19.— Similar to Fig. 18 (*bottom*) plot, but for different Z (height above the Galactic plane) bins ranging from $0.1 < Z/kpc < 0.4$ (*top left*) to $2.6 < Z/kpc < 3.6$ (*bottom right*). The sampled range of average semi-major axes and angular separations is given for each panel. In the $0.1 < Z/kpc < 0.4$ bin (*top left*), the upper limit on $\log(a_{break})$ is 3.50.

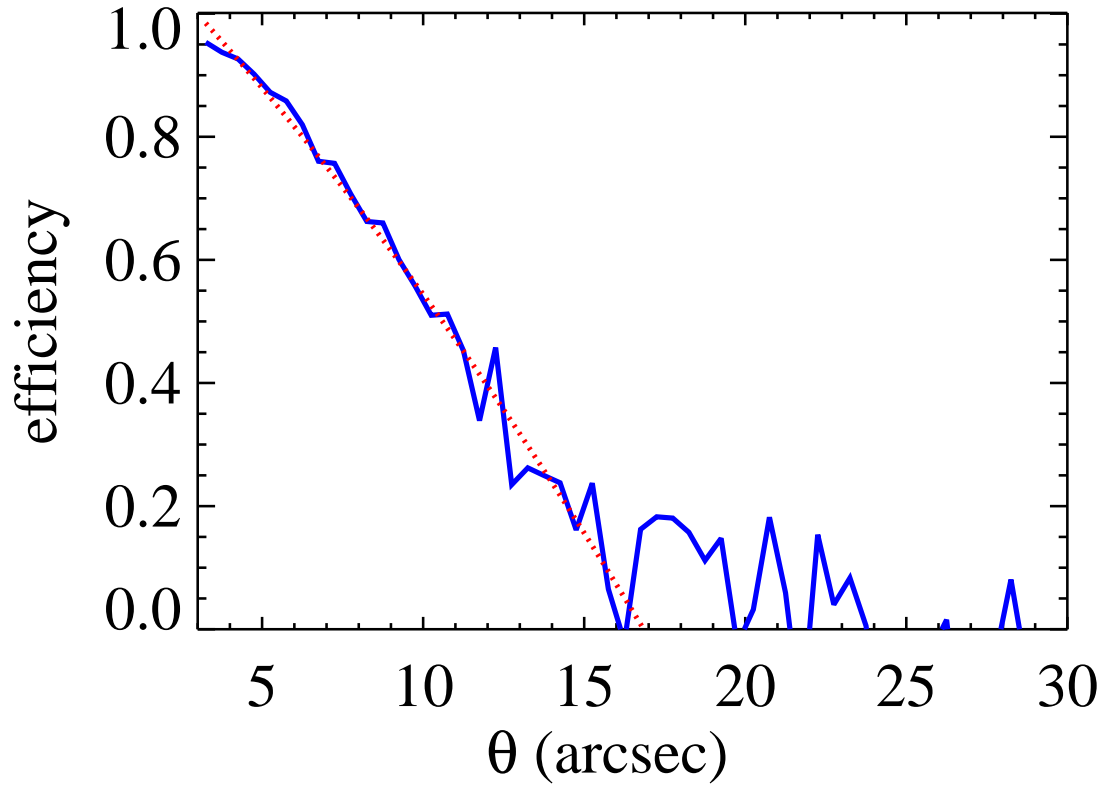


FIG. 20.— The fraction of true binaries (ϵ) in the $0.1 < Z/kpc < 0.4$, $|\delta| < 0.2$ geometrically-selected sample as a function of angular separation. The fraction goes below $\sim 5\%$ at $\theta_{max} = 16''$, and puts the upper limit on probed semi-major axes to $\sim 3,200$ AU.

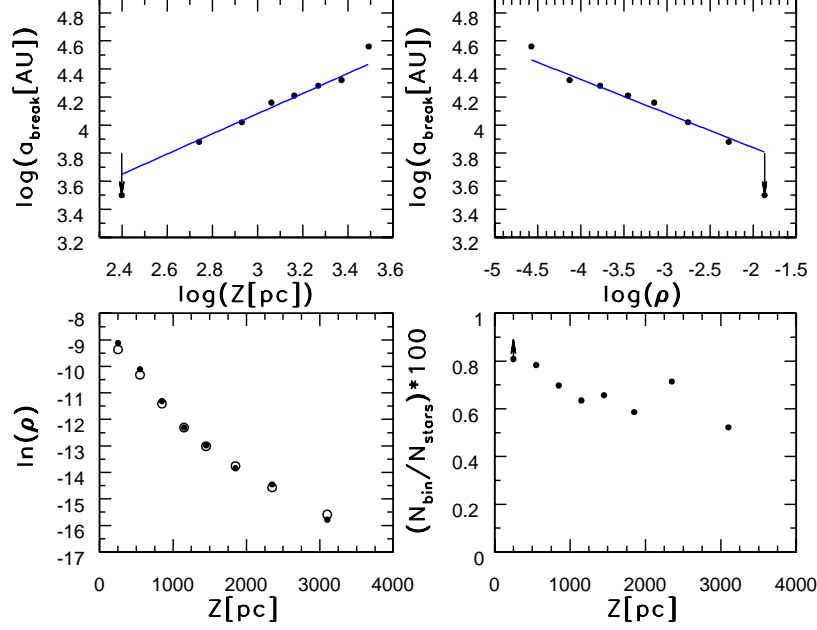


FIG. 21.— *Top left:* The dependence of $\log(a_{\text{break}})$ values (c.f. Fig. 19) on $\log(Z)$ (dots) is modeled as $\log(a_{\text{break}}) = k \log(Z) + l$, where $k = 0.72 \pm 0.05$ and $l = 1.93 \pm 0.15$, or approximately, $a_{\text{break}}[\text{AU}] = 12,302 Z[\text{kpc}]^{0.72}$. The symbol size shows the range between $\log(a_{\text{low}})$ and $\log(a_{\text{high}})$. The arrow indicates that the $\log(a_{\text{break}})$ in the $0.1 < Z/\text{kpc} < 0.4$ bin ($\log(Z) \sim 2.4$) is an upper limit. *Top right:* The dependence of $\log(a_{\text{break}})$ on $\log(\rho)$, where ρ is the local number density of stars, is modeled as $\log(a_{\text{break}}) = k \log(\rho) + l$, where $k = -0.24 \pm 0.02$ and $l = 3.35 \pm 0.07$, or $a_{\text{break}} \propto \rho^{-1/4}$. *Bottom left:* The dependence of local number density, $\ln(\rho)$, of binaries (dots) and stars (circles) on the height above the Galactic plane, where the density of stars is normalized to match the density of binaries at 1 kpc. *Bottom right:* The fraction of binaries relative to the total number of stars as a function of the height above the Galactic plane. The arrow shows the predicted fraction of binaries in the $0.1 < Z/\text{kpc} < 0.4$ bin, if the a_{break} value follows the $a_{\text{break}} \propto Z^{0.72}$ relation.

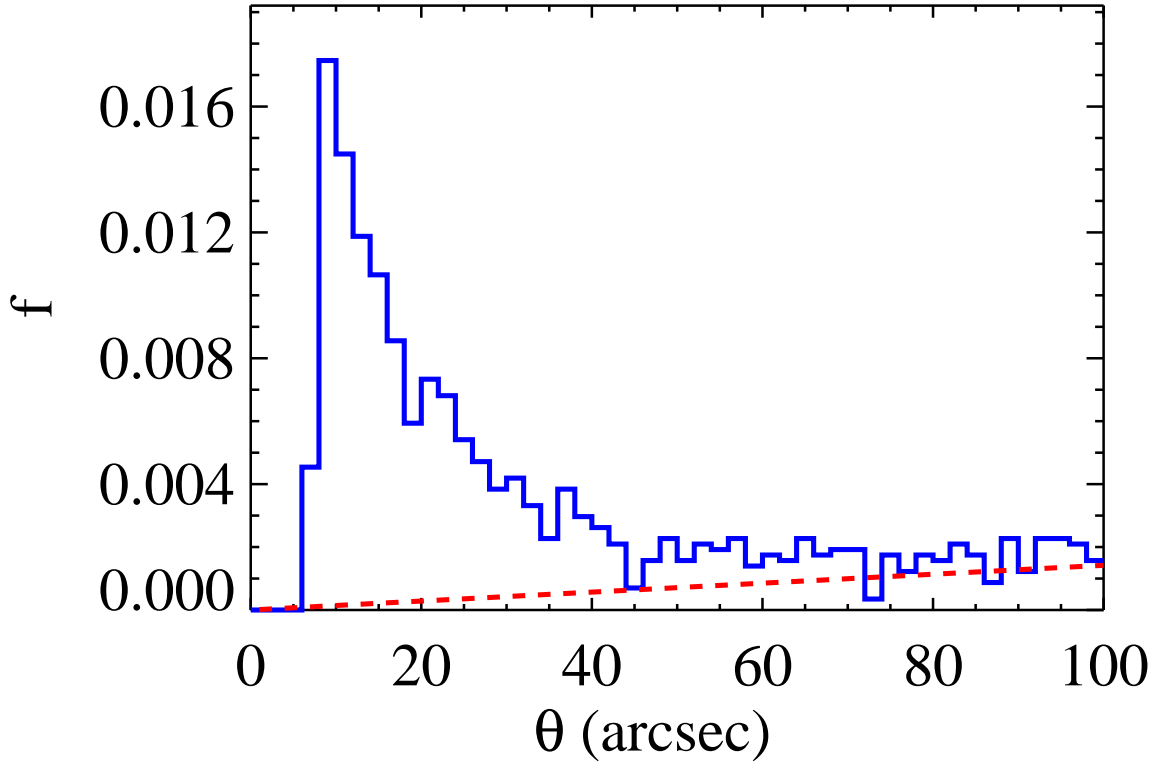


FIG. 22.— The distribution of angular separation for the $0.1 < Z/kpc < 0.4$, $|\delta| < 0.2$ kinematically-selected sample of candidate binaries. The data (*solid line*) extend to $\theta = 500''$, though the plotted range is restricted for clarity. The distribution of random pairs (*dashed line*) was obtained by fitting $f_{rnd}(\theta) = C\theta$ to the observed histogram for $\theta > 200''$. The sharp drop-off in the observed distribution for $\theta \lesssim 9$ is probably due to blending of close pairs in the POSS data.

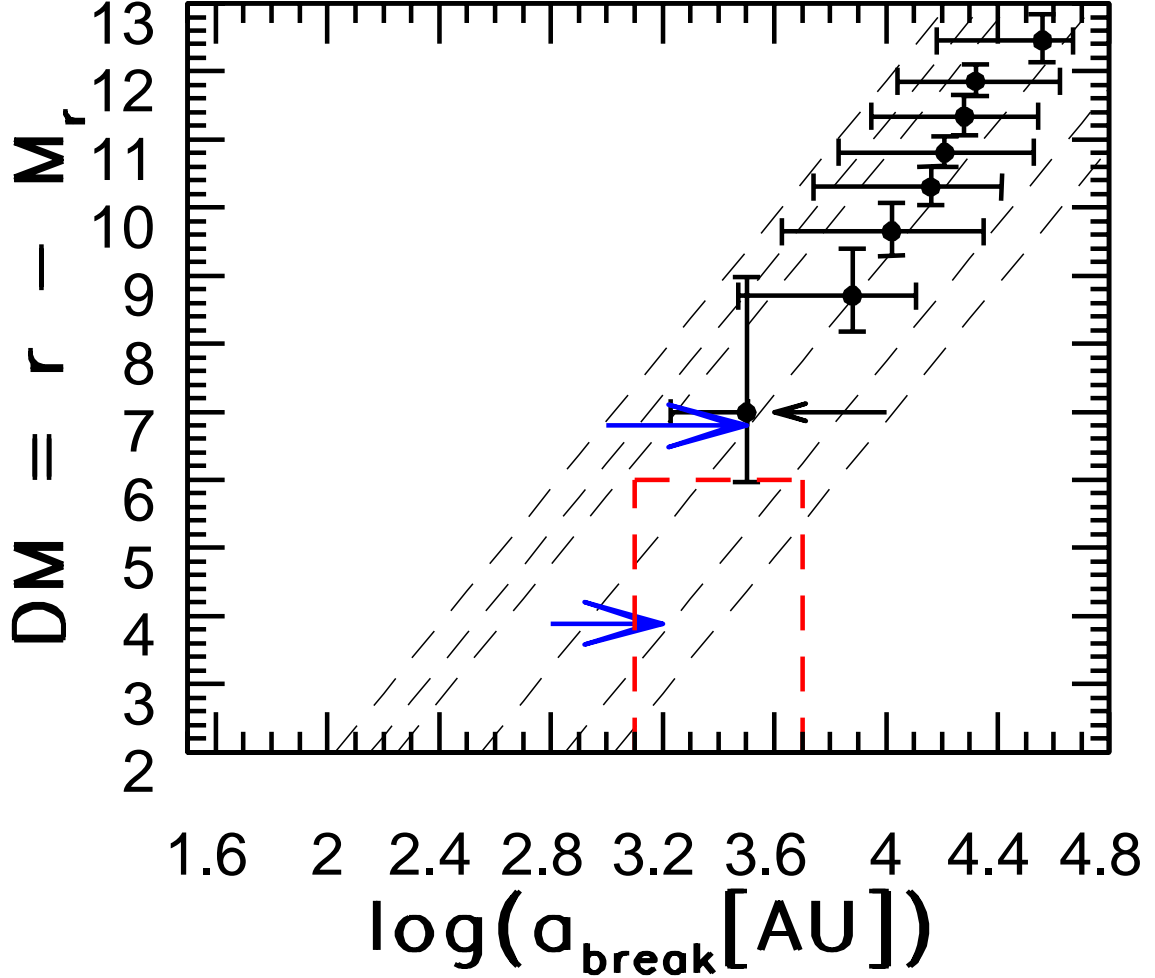


FIG. 23.— A comparison of results for the turnover in the distribution of semi-major axes, a_{break} , as a function of distance modulus, of wide binary systems determined here (symbols with error bars; the horizontal bars mark the range of probed semi-major axes, and the vertical bars mark the width of the distance bins; the lowest point is only a lower limit, for the sake of comparison with other results we ignore the difference between distance from us and distance from the Galactic plane because our sample is dominated by high galactic latitude stars), determined by Lépine & Bongiorno (2007; the dashed rectangle indicates constraint on a_{break} and the probed distance range), and determined by Chanamé & Gould (2004; big arrows, indicating upper limits on a_{break} and the probed distance range; the point at larger distance modulus corresponds to halo binaries). The diagonal dashed lines are lines of constant angular scale, θ , for values of $3''$, $4''$, $5''$, $10''$, $20''$ and $30''$ (from left to right).

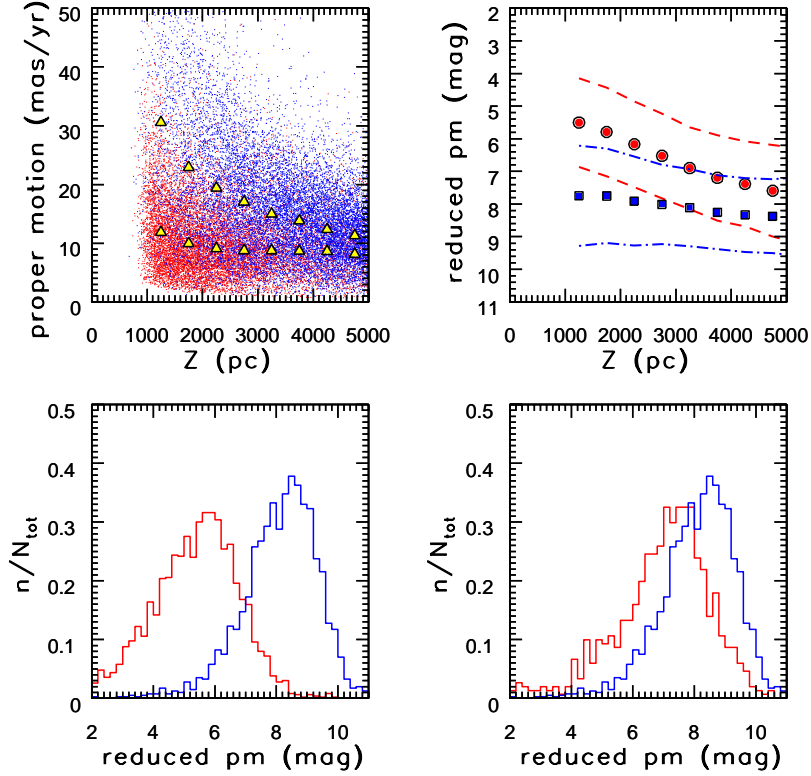


FIG. 24.— The top left panel shows the proper motion distribution as a function of distance from the Galactic plane (Z) for a sample of $\sim 16,000$ likely disk stars (red dots) and a sample of $\sim 34,400$ likely halo stars (blue dots). All stars have $14 < r < 20$ and $0.2 < g - r < 0.4$, and are separated using photometric metallicity. The triangles show the median values in 500 pc wide Z bins for each sample (lower symbols: disk, upper symbols: halo). Note that the median proper motion for disk stars becomes constant beyond $Z \sim 2$ kpc due to the vertical gradient of rotational velocity for disk stars. The top right panel shows the median position (symbols) and widths (lines; $\pm 1\sigma$ envelope around the medians) of the reduced proper motion sequences for disk (red dots and dashed lines) and halo (blue squares and dot-dashed lines) stars, as functions of Z . The two bottom panels show the cross-sections of the reduced proper motion sequences for stars with $Z = 1 - 1.5$ kpc (bottom left; red histogram for disk stars and blue for halo stars) and $Z = 3.5 - 4$ kpc. The histograms are normalized by the total number of stars in each subsample. The disk-to-halo star count ratio is 4.3 in the left panel, and 0.38 in the right panel. Note the significant overlap of the two sequences for large Z .

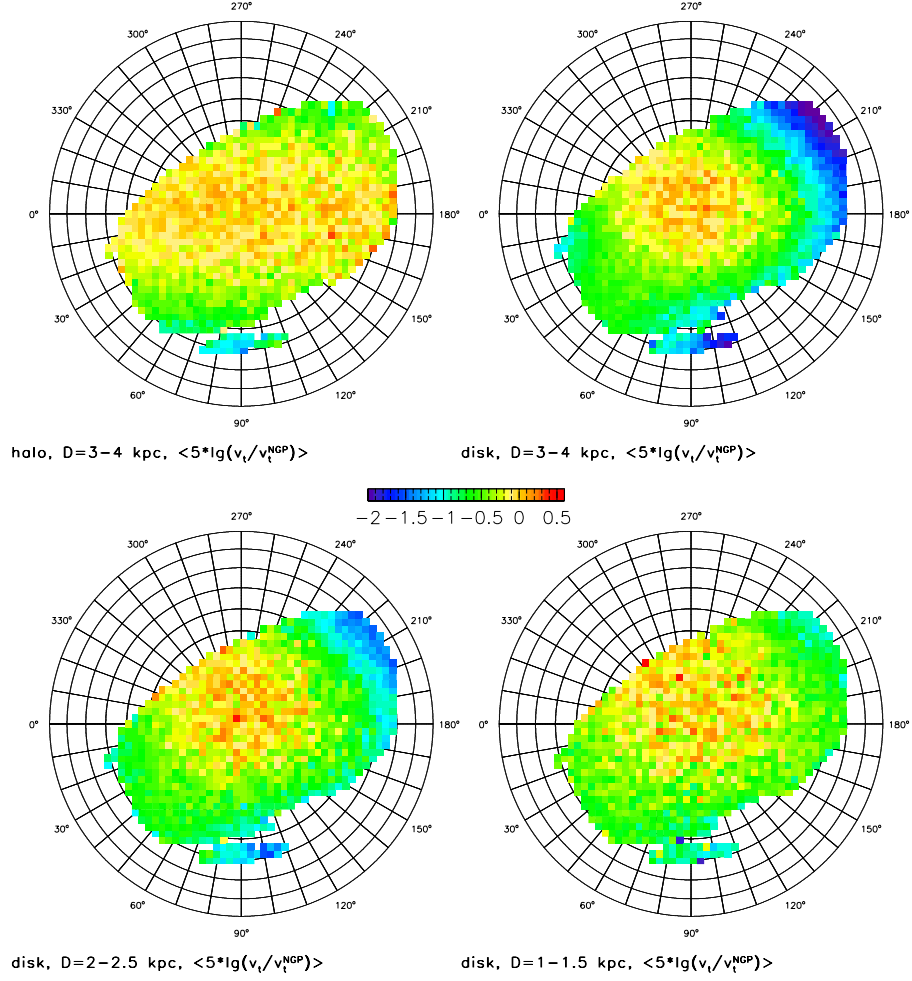


FIG. 25.— An illustration of the offsets in the position of reduced proper motion sequences as a function of distance, position on the sky and population. Each panel shows the median value of $5 \log(v_t/v_t^{NGP})$, where v_t is the heliocentric tangential velocity, and v_t^{NGP} is its value at the north Galactic pole, in Lambert projection of northern galactic hemisphere. The maps are color-coded according to the legend shown in the middle of the figure (magnitudes), and are constructed using stars with $0.2 < g - r < 0.4$. Stars are separated into halo and disk populations using photometric metallicity (for details see I08a). The top left panel shows results for halo stars with distances in the 3-4 kpc range. The other three panels correspond to disk stars in the distance range 3-4 kpc, 2-2.5 kpc, and 1-1.5 kpc.

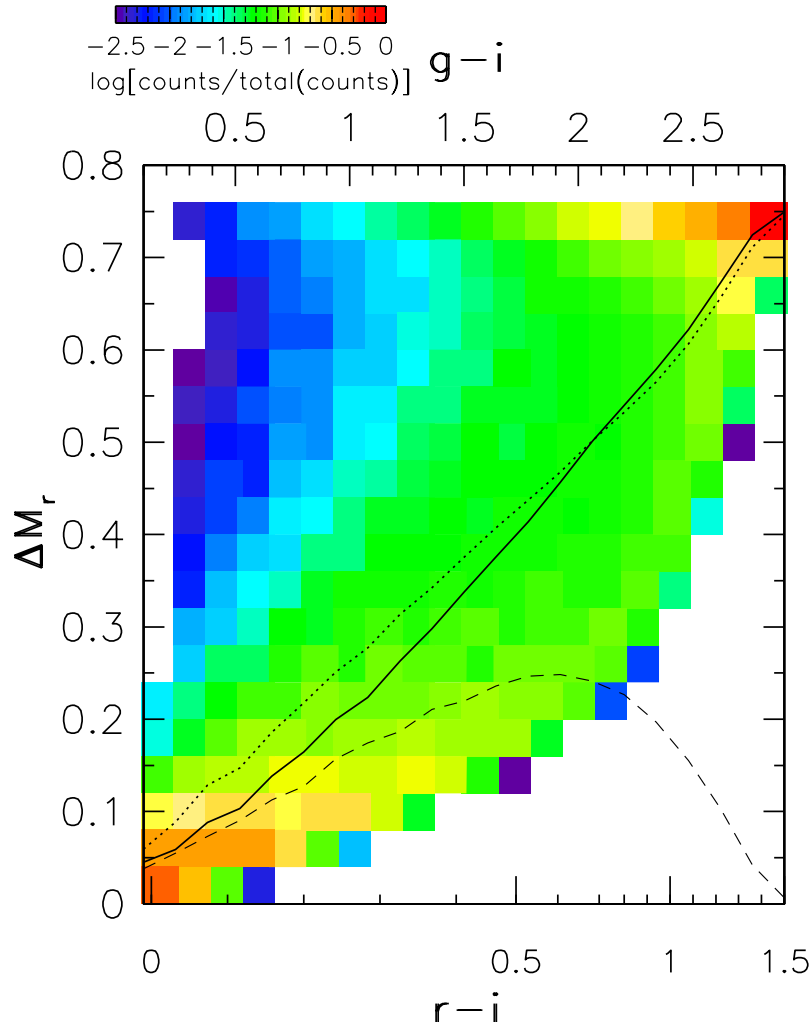


FIG. 26.— The number of unresolved binary systems (normalized with the total count in a given $g-i$ bin) with a magnitude offset $\Delta M_r = M_r(\text{assumed}) - M_r(\text{true})$ as a function of the system's $g-i$ color. The assumed absolute magnitude for a system with a $g-i$ color, $M_r(\text{assumed})$, was calculated using Eq. 15 (Eq. 1 from J08), while the true absolute magnitude, $M_r(\text{true})$ was calculated by adding up luminosities of components. The mean, median, and the rms scatter of ΔM_r are shown with the dotted, solid, and dashed lines, respectively.

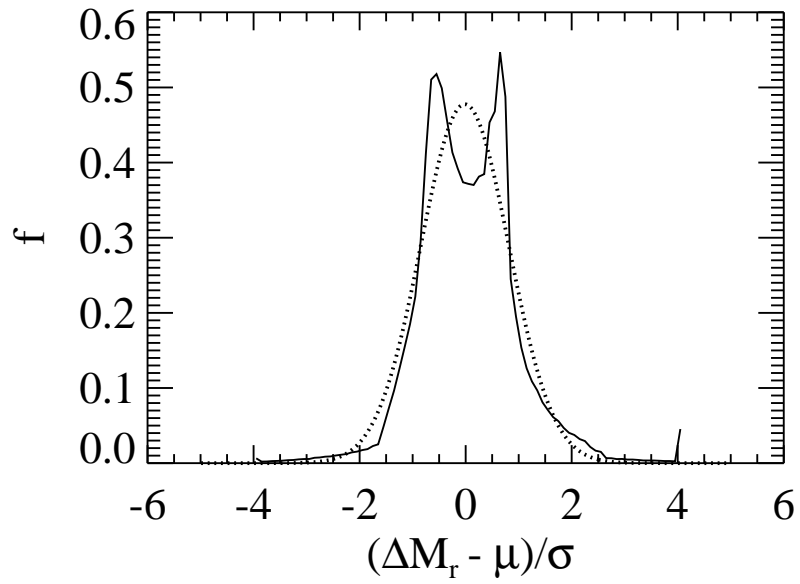


FIG. 27.— Distribution of differences between the magnitude offset, ΔM_r , and the median magnitude offset, μ , normalized with rms scatter, σ , (*solid line*) can be modeled as a 0.9 wide Gaussian (*dotted line*).

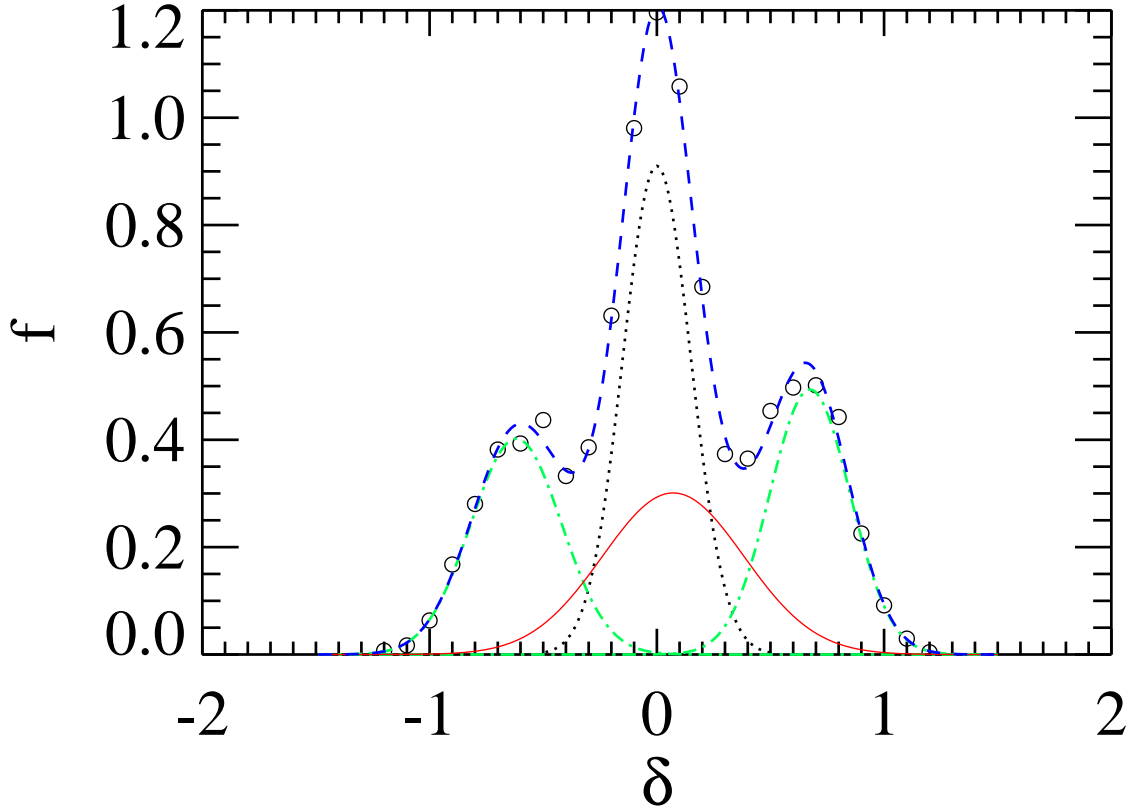


FIG. 28.— The distribution of δ values for the mock sample of wide binaries with both components redder than $g - i = 2.0$ (*open circles*). In this sample, a star has a 40% probability to be an unresolved binary system. Single star-single star configurations contribute the central narrow Gaussian (*dotted line*), unresolved binary-unresolved binary configurations contribute the central wide Gaussian (*thin solid line*), while the single star-unresolved binary configurations contribute the left and the right Gaussians (*dot-dashed lines*). The centers, widths, and areas of Gaussians are: $N_1(0.00, 0.15, 0.34)$, $N_2(0.06, 0.35, 0.28)$, $N_3(-0.64, 0.18, 0.18)$, $N_4(0.71, 0.17, 0.19)$ for the narrow, wide, left, and right Gaussians, respectively.